In-flight anti-icing simulation of electrothermal ice protection systems with inhomogeneous thermal boundary condition

Esmaeil Esmaeilifar[a], B. Sengupta[a], L. Prince Raj[b], R.S. Myong[a,*]

[a]School of Mechanical and Aerospace Engineering, and ACTRC, Gyeongsang National University, 501 Jinjudaero, Jinju, Gyeongnam 52828, South Korea

[b]Department of Aerospace Engineering and Applied Mechanics, Indian Institute of Engineering Science and Technology, Shibpur, Howrah,711103, India

*Corresponding author. E-mail address: *myong@gnu.ac.kr* (R.S. Myong)

Abstract

Conventional anti-icing computational solvers calculate the convective heat transfer coefficient using a homogeneous thermal boundary condition, assuming a constant temperature across the surface. However, this approach can lead to inaccuracies in regions with significant temperature variations. To address this limitation, the present study proposes a novel approach that utilizes an inhomogeneous thermal boundary condition, which updates the convective heat transfer coefficient based on the transient wall temperature distribution. We developed a unified finite volume framework that efficiently integrates various in-house solvers, including a compressible Navier-Stokes-Fourier (NSF) airflow solver, a Eulerian droplet impingement solver, a PDE-based ice solver, and a multilayer heat conduction solver. Thermal interaction between the different solvers was modeled using the conjugate heat transfer method. The effects of updating airflow on anti-icing results were investigated by comparing the results obtained by coupled and decoupled solvers. While the decoupled solver computes airflow once and remains unchanged, the coupled solver updates the airflow during the anti-icing simulation. Our findings show that the decoupled solver has the highest deviations from the coupled solver in evaporative anti-icing regimes, where dry regions form within the protection limits. Using coupled solvers in designing ice protection systems in evaporative regimes improves temperature prediction accuracy, enabling designers to reduce safety factors and save energy.

Keywords: Aircraft icing; electrothermal anti-icing; conjugate heat transfer; inhomogeneous boundary condition

1. Introduction

Aircraft icing occurs when an aircraft flies through icing clouds and encounters supercooled water droplets on its surface [1-3]. This can lead to ice accretion on critical components like the wing, engine, Pitot tube, and cockpit windows [4-9]. Ice accretion can reduce aerodynamic performance, increase drag, degrade stability and handling quality, and affect engine thrust production [10-13]. Developing reliable ice protection systems (IPS) is crucial to ensure the safety of flights in icing conditions [14-17]. Anti-icing and de-icing are the two main approaches used to protect aircraft in icing conditions. Anti-icing systems aim to prevent the accumulation of ice on aircraft surfaces. In contrast, de-icing systems allow some ice accretion on the surface but remove the ice before it causes notable aerodynamic penalties [18].

Various ice protection systems have been developed. Among them, bleed air, electrothermal heaters, electro-mechanical impulse systems, and pneumatic boot inflation are the most common types of IPS in the industry. Electrothermal IPS has emerged as the most popular choice in recent years due to its compatibility with the trend toward more electric aircraft. Initially, this technology was primarily employed for protecting helicopter blades, propellers, and pitot tubes. However, with the introduction of the electrothermal wing IPS in the Boeing 787, it has emerged as the primary ice protection system for the aircraft. The electrothermal IPS employs independent heating pads that feature automatic and adjustable input power, allowing for sequential activation and deactivation of the heater pads, which facilitates customized heat distribution on aircraft surfaces. This approach enables anti-icing and de-icing strategies, and can also be employed as a hybrid IPS in conjunction with emerging passive IPS. Passive IPS refers to strategies that mitigate ice accretion on the aircraft surface without relying on external energy sources or active control mechanisms [19]. This can be achieved using a superhydrophobic coating, which uses low-energy surfaces to repel the supercooled water droplets impinging on the coated surface or to facilitate the shedding of ice from the surface by lowering adhesion between the ice and surface.

Thermal anti-icing systems can function in three modes: fully evaporative, evaporative, and running wet [20]. In the fully evaporative mode, all incoming water evaporates near the impingement limits, resulting in a dry surface outside the impingement limits. In the second mode, called evaporative, water flows over the airfoil's leading edge and evaporates before reaching the end of the protected area. Finally, in the running wet mode, runback water flows beyond the protection limits, resulting in ice accretion in unprotected areas (runback ice). The runback water flow on the surface characterizes the anti-icing regime and is schematically illustrated in Fig.1.
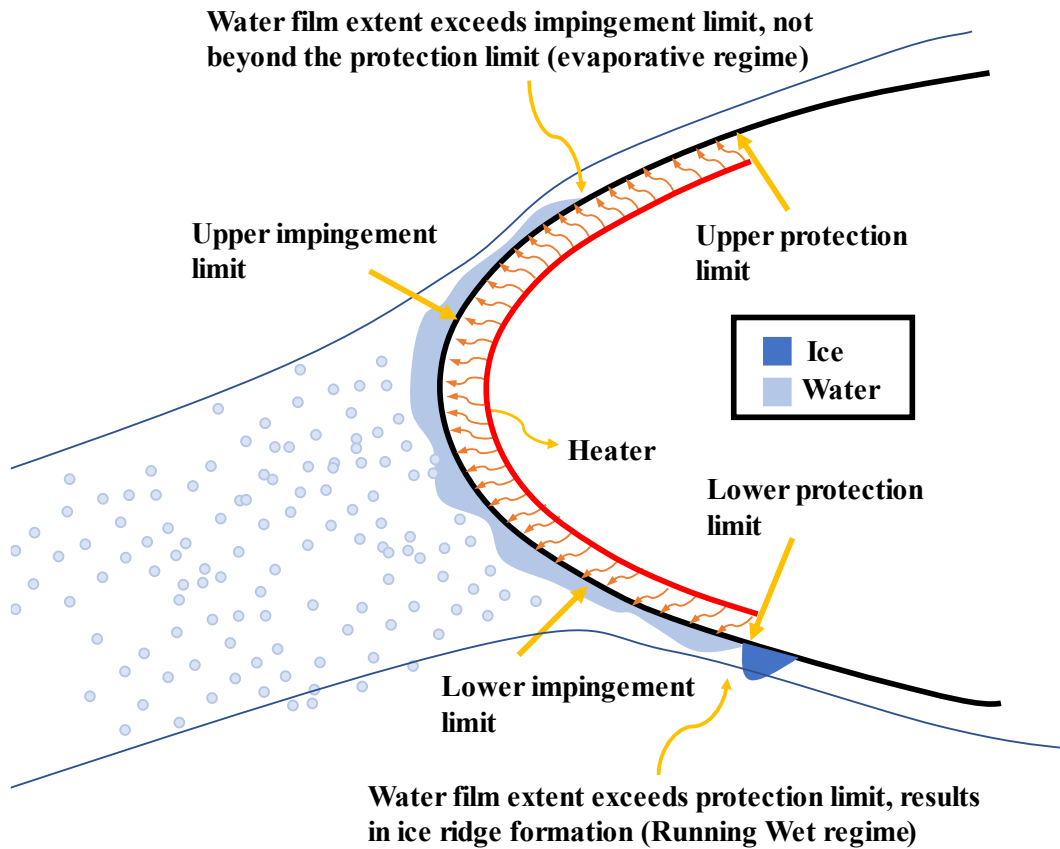
Fig. 1. Schematic illustration of the anti-icing regimes based on water film extent, impingement limits, and protection limits.

In-flight icing is a highly complex multiphysics process, and conducting experimental tests to investigate it is extremely limited due to its high costs, scalability issues, and the limited availability of test facilities [21]. As an alternative, developing accurate and reliable numerical models can decrease

costs and speed up the preliminary design and certification process [22]. At the same time, these codes can be used to reveal the underlying physics behind the process and to optimize the IPS design for more energy-efficient systems [23-26]. The computational simulation of electrothermal IPS requires a comprehensive multiphysics framework, employing different solvers to model a range of physical phenomena. Such a solver should be accurate, robust, reliable, and efficient. In the context of anti-icing simulation, accuracy refers to minimizing the deviation of wall temperature predictions from the experimental values within an acceptable range. Robustness refers to the numerical stability of the coupling strategy employed at the interface of the coupled solvers. Reliability means that the solver can predict accurate results in a wide range of flight and icing conditions. Finally, for a given level of accuracy, efficiency refers to the numerical model that requires the least computational resources.

The air solver simulates airflow around the flying vehicle to predict the heat transfer coefficient and wall shear stress. The droplet solver simulates the air-mixed water droplet flow field to calculate the distribution of droplets and predict the impingement characteristics of the body. A thermodynamic solver is also required to predict the runback water film and ice accretion/melting on the surface using mass and energy conservation equations. Finally, the heat conduction solver calculates the temperature distribution inside and on the surface of the multilayered composite medium [14]. Computationally simulating aircraft anti-icing problems involves different domains of air/droplet, solid, and water/ice. Considering thermal interactions between different domains requires special numerical modeling to couple the different solvers corresponding to each domain. Information between the solid and fluid domains is exchanged at the interface utilizing the conjugate heat transfer (CHT) method [27, 28].

Table 1 compares different models that have been developed to simulate electrothermal anti-icing problems. Traditional anti-icing solvers use the Euler equations or panel methods to simulate airflow, along with the integral boundary layer (IBL) approach, to predict the convective heat transfer coefficient (CHTC) and wall shear stress on the wall [20, 29-33]. These solvers usually employ the Messinger

4

thermodynamic model to solve for the runback water film on the surface. This approach does not consider water accumulation on the surface, since it assumes that all unfrozen water in the cell flows to the adjacent cell. This model also needs to calculate the stagnation point on the wall, which makes it complicated for complex 3D shapes. Moreover, traditional anti-icing solvers usually use equivalent thermal conductivity to avoid solving heat conduction in the composite. Energy conservation on the airfoil surface focuses solely on conduction along the surface, disregarding conduction perpendicular to it due to the thinness of the heating elements. The effective thermal conductivity of the underlying material can be approximated using an electrical analogy, considering the thermal resistance of the materials composing the heating element from the heater to the outer surface at the top [21]. While this approach neglects heat conduction perpendicular to the surface, it can be beneficial for cases where detailed information about the solid region is not available.

ANTICE [22] adopts the IBL method used in LEWICE to predict the CHTC in anti-icing problems. Considerable disparities concerning solid surface temperatures were observed between the numerical outcomes and experimental data, and so the authors enabled direct usage of the experimental heat transfer coefficient within the ANTICE code. Even when measured laminar heat transfer coefficients were used, it resulted in a mismatch between the numerical results and the experimental data for surface temperature. The reason is that during wet experiments, laminar flow is disturbed by rivulet and bead formation in the runback water. This results in a transition from laminar to turbulent flow, which causes a sensible change in the heat transfer coefficient. They manually tripped the flow in dry air experiments to modify the heat transfer coefficient measured from dry air, to mimic the flow behavior in a wet simulation [22].

Table 1
Comparison of different anti-icing solvers available in the literature.

	Airflow	Composite modeling	Turbulent transition	Runback water	CHTC calculation method
ANTICE [32, 34]	Potential flow	FDM	-	Messinger	Airflow is fixed, and CHTC is calculated using isothermal wall temperature.

Silva [20, 29, 30]	Euler + IBL	Equivalent thermal conductivity	Empirical intermittency function	Messinger	Airflow is fixed, and transient T_{wall} is used to update CHTC using IBL.
Bu et al. [35]	NSF	FVM	-	Messinger	Airflow is updating, transient T_{wall} is used to update CHTC using RANS.
PoliMIce [21]	Euler + IBL	Equivalent thermal conductivity	Empirical intermittency function	Lubrication theory	Airflow is fixed, and transient T_{wall} is used to update CHTC using IBL.
Shen et al. [36]	NSF	FVM	-	Messinger	Airflow is fixed, and CHTC is calculated using isothermal wall temperature.
Present (all in-house codes)	NSF	FVM	Transitional Spallarat-Allmaras turbulence model	PDE	Airflow is updating, and transient T_{wall} is used to update CHTC using RANS.

Morency et al. [33] incorporated the finite difference method (FDM) to predict heat and mass transfer around the wing. Using an intermittency function, they considered laminar, transitional, and turbulent boundary layers. Silva et al. [20, 30] developed a numerical code to model electrothermal anti-icing problems. They evaluated momentum and thermal boundary layers based on non-isothermal surface temperature in laminar, turbulent, and transitional flow regimes. In this approach, they considered a smooth transition from laminar to turbulent flow. The convective heat transfer coefficient (CHTC) was updated by altering wall temperature using the IBL method which strongly depends on the empirical data. Later, they developed a model to predict rivulet and bead formation in runback water film in terms of wetness factor, which can enhance the heat transfer on the surface [29]. Their model could predict the onset position of the laminar-to-turbulent position and the length of the transitional region based on the pressure gradient and turbulence level effects. However, they did not consider ice formation in unprotected areas, which can happen when running wet anti-icing mode or with the failure of IPS. Recently, Gutiérrez et al. [21] developed a computational model for the electrothermal anti-ice systems based on Silva's model. Specifically, they enhanced the liquid film model utilizing lubrication theory and incorporated ice formation in the anti-ice model, which was not present in Silva's initial model.

The new generation of anti-icing solvers employs CFD solvers along with turbulence models to predict the airflow and calculate the CHTC and wall shear stress on the surface. This approach eliminates the

need for boundary layer models, which greatly depend on empirical relations. The new solvers also use the Eulerian method to predict droplet impingement by solving shallow water-type droplet equations. Eulerian methods [37-39] are robust compared to conventional Lagrangian models, which are less robust when it comes to tracking droplets in complex 3D problems. In addition, Bourgault et al. [40] also introduced a PDE-based thermodynamic model that utilizes lubrication theory to solve mass and energy conservation equations for runback water film. This model, known as the shallow water icing model (SWIM), considers the wall shear stress to be the main driving force of runback water film on the surface. Incorporating these new approaches increases versatility and applicability across various scenarios.

In most anti-icing tools, airflow simulation is not updated during the anti-icing simulation. In other words, the CHTC is calculated based on a homogenous thermal boundary condition (isothermal wall temperature), and its value remains unchanged during the anti-icing simulation. However, the surface temperature distribution changes during the simulation, which can significantly alter the CHTC, especially in the aft region of the leading edge. Any change in convective heat transfer affects the heat balance in the thermodynamic ice solver, eventually resulting in different temperature predictions. For instance, Shen et al. [36] employed temperature-based and flux-based approaches to perform anti-icing simulations. They used an NSF solver along with the Spalart-Allmaras (SA) turbulence model to predict the CHTC based on a homogeneous thermal boundary condition (isothermal wall temperature). The airflow simulation was carried out once, keeping the CHTC unchanged during the anti-icing simulation. The flux-based approach directly calculates the surface temperature in the ice solver without any further assumption. On the other hand, the temperature-based approach assumes that temperature is a known variable and phase change occurs in an artificial temperature range around the critical temperature [36].

Studies that address the challenge of updating airflow in anti-icing simulation are limited. Based on the commercial SW ANSYS FLUENT, Bu et al. [35] improved the temperature-based coupling approach to update the airflow during anti-icing simulation. In their approach, air/conduction coupling calculates

the temperature which is further corrected by the heat load computed in the ice solver. The main issue with the temperature-based approach is that airflow and conduction solvers do not have any sense of phase change that happens in the ice solver. As a result, the coupling time step between the runback solver and air/conduction solvers should be small enough to ensure that the change in surface temperature is not larger than the artificial phase change temperature. Otherwise, the thermodynamic solver can jump from the rime ice region to the water film region without entering the glaze region. They also utilized the Messinger model for the runback water film, which assumes that all unfrozen water in the cell flows to the adjacent cell. As a result, it does not consider water accumulation in the cell.

This study presents a novel approach for updating airflow in anti-icing simulations, overcoming the limitations of previous methods. Our approach utilizes an inhomogeneous thermal boundary condition to update the CHTC based on the transient wall temperature distribution. We carefully selected the coupling strategies between different solvers to ensure maximum alignment with the physics involved in the anti-icing problem.

First, we compute the surface temperature in ice/conduction coupling and correct it with the updated CHTC from airflow. It aligned with the physics of the problem where ice and conduction have higher thermal interaction compared to the air solver. Second, we use a flux-based approach, which directly calculates the surface temperature in the ice solver without the need for further assumptions for phase change temperature. Third, we employ a modular approach in which all solvers operate independently, and the time step for each solver can be calculated separately based on their corresponding physical time scales.

The main novelties of this study are twofold. *First, we developed a new approach for updating airflow in anti-icing simulations using an inhomogeneous thermal boundary condition, which overcomes the limitations of previous solvers. Second, we investigated the effects of updating airflow on anti-icing results, including wall temperature distribution and runback ice shape, which, to the best knowledge of*

the authors, have not been studied before. The findings of this study can help designers determine the scope and conditions under which results obtained by decoupled solvers are reliable. It also indicates where caution is necessary when using decoupled solvers for designing and analyzing anti-icing systems. To investigate the effects of updating airflow on the anti-icing results, we developed two solvers: A coupled solver and a decoupled solver. While the coupled solver updates the airflow during the anti-icing simulation, in the decoupled solver, airflow simulation is conducted once and remains unchanged during the simulation. The coupled solver utilizes inhomogeneous thermal boundary conditions in an unsteady air solver to update the CHTC based on the transient wall temperature distribution calculated in the ice/conduction solver. On the other hand, the decoupled solver calculates the CHTC using homogeneous thermal boundary conditions (constant isothermal wall) and remains unchanged during the anti-icing simulation. Updating the CHTC based on the inhomogeneous thermal boundary condition could provide accurate results for wall temperature distribution and runback ice formation.

Table 2
Comparison of present coupled and decoupled in-house anti-icing solvers.

	Airflow	**Thermal BC**	**CHTC**
Decoupled Solver	Steady-State	Homogenous	Remain unchanged during Anti-icing simulation
Coupled Solver (Novel)	Transient	Inhomogeneous	Updates based on transient wall temperature

Both coupled and decoupled solvers developed in this study utilize the transitional Spalart-Allmaras turbulence model to predict the CHTC in laminar, turbulent, and transitional flows. In addition, a time-accurate, unsteady solver with a dual time-stepping temporal scheme was used to utilize unsteady simulations with acceptable accuracy and efficient computational cost. The numerical results obtained by present coupled and decoupled solvers are compared with experimental data at four test cases that cover different anti-icing regimes, including fully evaporative, evaporative, and running wet anti-icing regimes. Finally, the effects of updating airflow on wall temperature distribution and runback ice shape

characteristics were studied under different icing and atmospheric conditions to include the effects of free stream temperature and velocity, LWC, and angle of attack.

2. Computational methodology

2.1. Overall procedure and flowchart

Two distinct solvers were developed to highlight the differences in the anti-icing results obtained from coupled and decoupled solvers. In the decoupled solver, an airflow simulation is conducted once using homogenous thermal BC and remains unchanged during the simulation, while in the coupled solver, the airflow results are updated by changing the wall temperature distribution using an inhomogeneous thermal boundary condition. As shown in Fig. 2, the decoupled solver, the simulation starts with a clean airflow simulation and a homogeneous boundary condition. Air flow-field data of density, velocity, and pressure fields are transferred to the droplet solver. In addition, wall shear stress and the convective heat transfer coefficient from the air solver, and the droplet collection efficiency from the droplet solver, are passed to the ice solver. Heat conduction through the solid is calculated in the heat conduction solver, which is tightly coupled with the ice solver.

The coupled solver is initiated in the same way as the decoupled solver, starting with a clean airflow simulation followed by a droplet impingement solver. The ice and conduction solvers are tightly coupled, providing a wall temperature distribution to the air solver as an inhomogeneous thermal boundary condition. In return, the unsteady air solver also updates the convective heat transfer coefficient based on the updated wall temperature distribution. The unsteady air solver is loosely coupled with the ice and conduction solvers, which means that there are no sub-iterations in the coupling process.

10
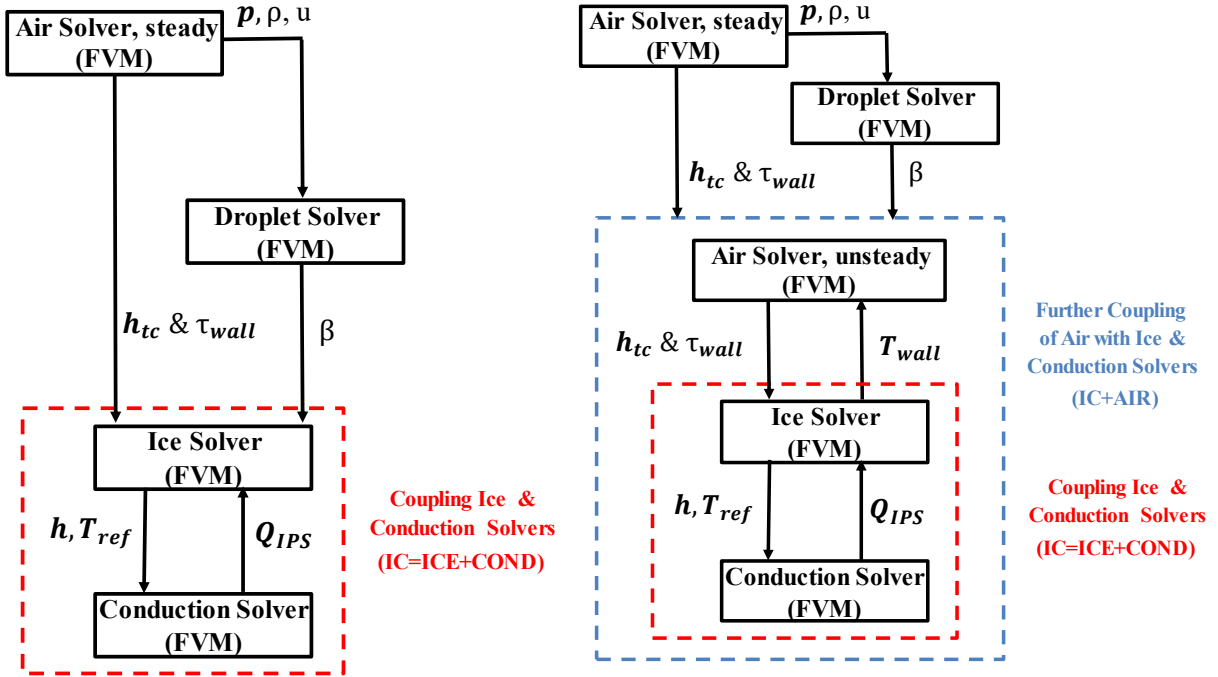
Fig. 2. Comparison of decoupled (left) and coupled (right) solvers pertinent to the simulation of ice protection systems.

2.2. Airflow solver

To simulate the airflow, a finite volume method is employed to solve the compressible Navier-Stokes-Fourier (NSF) equations, which are as follows:

$$
\begin{bmatrix} \rho_a \\ \rho_a \boldsymbol{u}_a \\ \rho_a E \end{bmatrix}_t + \nabla \cdot \begin{bmatrix} \rho_a \boldsymbol{u}_a \\ \rho_a \boldsymbol{u}_a \boldsymbol{u}_a + p\boldsymbol{I} \\ (\rho_a E + p)\boldsymbol{u}_a \end{bmatrix} = \nabla \cdot \begin{bmatrix} 0 \\ \boldsymbol{\tau} \\ \boldsymbol{\tau} \cdot \boldsymbol{u}_a + \boldsymbol{Q} \end{bmatrix}, \tag{1}
$$

$$
\boldsymbol{\tau} = 2\mu \left[\nabla \boldsymbol{u}_a \right]^{(2)}, \; \boldsymbol{Q} = k\nabla T, \; E = h - \frac{p}{\rho_a} + \frac{\boldsymbol{u}_a \cdot \boldsymbol{u}_a}{2}, \tag{2}
$$

where τ and Q represent the non-conserved variables corresponding to viscous shear stress and heat flux, respectively. $\left[\nabla \boldsymbol{u}_a \right]^{(2)}$ stands for the traceless symmetric part of $\nabla \boldsymbol{u}_a$. Also, E represents the total energy density. The ideal equation of state $p = \rho_a RT$ is employed to close the conservation laws (1). It is worth mentioning that the air solver was parallelized using the Message Passing Interface (MPI) library to enable expensive unsteady simulations of the air solver in an acceptable computational time [41].

11

Moreover, a Dirichlet-type inhomogeneous thermal boundary condition was applied at the wall to consider transient wall temperature distribution during the anti-icing simulation.

2.2.1. Dual time-stepping

Utilizing the method of lines, the governing equations of the air solver are discretized separately for space and time, which leads to a system of coupled ordinary differential equations in time, as follows:

$$\frac{d(\Omega \vec{W}_I)}{dt} = -\vec{R}_I,$$
(3)

where Ω, W, and R denote the volume, conserved variables, and residual, respectively. An explicit multi-stage Runge-Kutta scheme is employed for the temporal discretization of Eq. (1). Local time stepping is used for steady air simulation to accelerate the convergence efficiently.

Moreover, the dual time-stepping approach is implemented in the air solver to perform an unsteady air simulation. This method breaks the time domain into a physical time step and a pseudo time step. The physical time is used to advance the solution in time with an explicit multi-stage Runge-Kutta scheme, while the pseudo time is used to converge the solution to a steady state at each physical time step by adding a pseudo time derivative term to the governing equations, as follows [42]:

$$\frac{d(\Omega \vec{W}_I^*)}{d\tau} + \frac{d(\Omega \vec{W}_I)}{dt} = -\vec{R}_I^*,$$
(4)

$$\vec{R}_I^* = \vec{R}_I + \frac{\Omega}{2\Delta t}(3\vec{W}_I^* - 4\vec{W}_I^n + \vec{W}_I^{n-1}),$$
(5)

where t and τ are the physical and pseudo times, respectively. A backward difference scheme is employed to discretize the physical time, and the solution is obtained by marching the equations in pseudo time. The pseudo-time derivative term is driven to zero by iterating in pseudo-time with an explicit scheme until a desired accuracy is reached. This method allows for larger physical time steps than the standard

explicit schemes while maintaining accuracy and stability, making it computationally efficient to solve expensive unsteady NSF equations [42, 43].

2.2.2. Laminar to turbulent transition

The FVM-based air solver couples the NSF equations with the one-equation SA turbulence model. This turbulence model is computationally efficient and works well for external flows, making it the most used turbulence model in the aircraft icing community. The Spalart-Allmaras turbulence model solves only one transport equation for kinematic eddy viscosity ($\tilde{v}$). The transitional version of the SA turbulence model was initially developed by Bas and Cakmakcioglu [44] (SA-BC model), which was recently modified as the SA-BCM model [45, 46]. This model considers the laminar to turbulent transition by multiplying an intermittency function (γ) to the production term of eddy viscosity in the transport equation, as follows:

$$\frac{\partial}{\partial t}(\rho \tilde{v}) + \frac{\partial}{\partial x_j}(\rho \tilde{v} u_j) = \gamma C_{b1} \rho \tilde{S} \tilde{v} + \frac{1}{\sigma}\left\{\frac{\partial}{\partial x_j}[\mu_L + \rho \tilde{v}]\frac{\partial \tilde{v}}{\partial x_j} + \rho C_{b2}\frac{\partial \tilde{v}}{\partial x_j}\frac{\partial \tilde{v}}{\partial x_j}\right\} - \rho C_{w1} f_w \left(\frac{\tilde{v}}{d}\right)^2, \tag{6}$$

$$\mu_T = \rho \tilde{v} f_{v1}. \tag{7}$$

In this equation, μ_T is the turbulent viscosity used to close the Reynolds-Averages Navier-Stokes equations. u_j and d are the components of mean flow velocity and distance from the closet wall. Other constants can be found in Ref. [47] since the noft2 version of the SA model with wall roughness is modified to implement the transition. The intermittency function is defined as follows:

$$\gamma = 1 - \exp(-\sqrt{Term1} - \sqrt{Term2}), \tag{8}$$

$$Term1 = \frac{\max(\text{Re}_\theta - \text{Re}_{\theta c}, 0.0)}{\chi_1 \text{Re}_{\theta c}}, \tag{9}$$

$$Term2 = \max(\frac{\mu_T}{\chi_2 \mu}, 0.0), \tag{10}$$

where χ_1 and χ_2 are constant values of 0.002 and 0.02, respectively. Re_θ and $\text{Re}_{\theta c}$ are given as:

$$\text{Re}_\theta = \frac{\rho d^2}{\mu} S,$$ (11)

$$\text{Re}_{\theta c} = 803.73(TI_\infty + 0.6067)^{-1.027}.$$ (12)

Here S and TI_∞ are the absolute values of vorticity and turbulent intensity. Intermittency function values range from zero to one, corresponding to laminar and fully turbulent regimes, respectively. *Term1* is mainly responsible for the value of γ and the onset location of transition. However, without *Term2* the intermittency function cannot grow inside the laminar boundary layer [46]. It should be noted that Reynolds-Averaged Navier-Stokes turbulence models rely on Reynolds averaging, where the averaging process inherently loses information about the small-scale fluctuations that are crucial for triggering the transition process.

To validate the transitional SA turbulence model (BCM model) implemented in the present solver, the numerical results of the friction coefficient were compared with experimental data from Schubauer and Klebanoff [48] and numerical results from the original implementation by Mura and Cakmakcioglu [46]. The test case is a natural transition over a flat plate in which free stream velocity is 50.1 m/s, the Reynolds number is 3.4 million, and a turbulent intensity of 0.18%. The computational domain extends from -1 to 4 m in the X direction and from 0 to 1m in the Y direction. A no-slip wall boundary condition is applied to the wall, starting from 0 to 1m in the X direction. The symmetry boundary condition is applied to the whole bottom boundary except for the wall. The far-field boundary condition is applied to the top, left, and right boundaries. The grid consists of 20,000 cells, 100 cells in the *y* direction and 200 cells in the *y* direction. The height of the first cell is adjusted to ensure *y+*<1 on the wall.
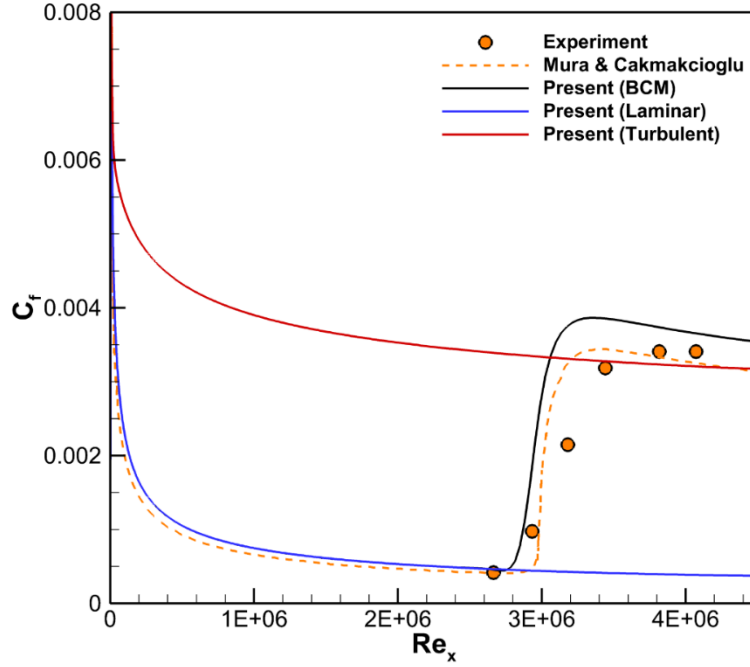
Fig. 3. Skin friction coefficient over a flat plate with a natural laminar to turbulent transition.

2.3. Droplet impingement solver

The domain of interest in the droplet solver is the air-mixed droplet flow field around the aircraft. Since the effect of water droplets on the airflow is negligible, a one-way coupling method is employed to predict the droplet impingement on the surface. In icing applications, the complex distribution of droplet sizes within clouds is often characterized by a single parameter, the median volume diameter (MVD). The MVD approach has proven useful since it simplifies calculations while providing a useful estimate for ice accretion simulations [49]. The current solver is a Eulerian-based model for solving shallow water-type droplet equations (SWDEs). The original SWDE equations are not strictly hyperbolic. This issue was resolved in the previous work by splitting the system into a source term and a well-posed part as follows [38]:

$$
\begin{bmatrix} \rho \\ \rho \boldsymbol{u} \end{bmatrix}_t + \nabla \cdot \begin{bmatrix} \rho \boldsymbol{u} \\ \rho \boldsymbol{u}\boldsymbol{u} + \rho g d \boldsymbol{I} \end{bmatrix} = \begin{bmatrix} 0 \\ A_{\boldsymbol{u}} \left(\boldsymbol{u}_a - \boldsymbol{u} \right) + \boldsymbol{S}_b + \nabla \cdot \left(\rho g d \boldsymbol{I} \right) \end{bmatrix}.
\tag{13}
$$

15

The air and droplet velocity components are represented by $\boldsymbol{u}$ and $\boldsymbol{u}_a$, respectively. S_b is an estimation of the gravity and buoyancy forces on the droplet. The aerodynamic drag on droplets due to the airflow is represented by the term $A_{\mathbf{u}}(\boldsymbol{u}_a - \boldsymbol{u})$. Finally, the term $\nabla \cdot (\rho g d \boldsymbol{I})$ is added to both sides of the momentum equation to resolve the non-strictly hyperbolic nature of the Eulerian droplet equations [38].

2.4. Ice accretion solver

The ice solver is a PDE-based thermodynamic model that solves mass and energy conservation equations for runback water on the surface. The current PDE-based model considers the rate of mass and energy change, which is missing in the algebraic Messinger model. It is worth mentioning that the wing's geometry does not change during the simulation since no ice should be formed on the protected areas in the anti-icing simulation. This model was developed based on lubrication theory since the height of the water film in aircraft icing applications is on the order of 10 μm. The ice solver calculates the equilibrium temperature (T_{equi}), water film thickness (h_f), and ice accretion rate ($\dot{m}_{ice}$) by solving the governing equations as follows [6]:

$$
\left[\begin{array}{c} h_f \\ h_f T_{equi} \end{array} \right]_t + \nabla \cdot \left[\begin{array}{c} \dfrac{h_f^2}{2\mu_w}\boldsymbol{\tau}_{wall} \\ \dfrac{h_f^2 T_{equi}}{2\mu_w}\boldsymbol{\tau}_{wall} \end{array} \right] = \left[\begin{array}{c} \dfrac{S_M}{\rho_w} \\ \dfrac{S_E}{\rho_w c_{p,w}} + \dfrac{T_C S_M}{\rho_w} \end{array} \right],
\tag{14}
$$

$$
S_M = \dot{m}_{imp} - \dot{m}_{evap} - \dot{m}_{ice},
$$

$$
S_E = \left[Cp_w \tilde{T}_{d,\infty} + \dfrac{\|\boldsymbol{u}_d\|^2}{2} \right] \times \dot{m}_{imp} - L_{evap}\dot{m}_{evap} + h_c \left(T_{equi} - T_\infty \right) + \dot{m}_{ice}\left[L_{fus} - Cp_{ice}T_{equi} \right] + \dot{Q}_{IPS},
\tag{15}
$$

$$
\dot{m}_{imp} = U_\infty LWC_\infty \beta.
$$

Here $\dot{m}_{imp}$ and $\dot{m}_{evap}$ are the instantaneous water droplet impingement mass and evaporation mass, respectively. Here, wall shear stress (τ_{wall}) and the convective heat transfer coefficient (h_c) are calculated

16

in the air solver, while collection efficiency (β) and droplet impact velocity ($\boldsymbol{u}_d$) are predicted in the droplet solver, and finally, heat flux ($\dot{Q}_{IPS}$) from the solid is estimated in the conduction solver.

2.5. Heat conduction solver

A heat conduction solver based on the FVM approach was developed to predict the temperature distribution inside the solid and on the surface of the multilayer composite, as follows:

$$\rho_s C_{p_s} \frac{\partial T}{\partial t} = \nabla \cdot (k_s \nabla T) + S(t), \tag{16}$$

where ρ_s, C_{p_s} and k_s are the density, specific heat, and thermal conductivities of each composite layer. Heater pads are placed between composite layers, and $S(t)$ represents the transient heater fluxes.

2.6. Coupling solvers using loose/tight conjugate heat transfer method

In this study, the ice and conduction solvers were tightly coupled due to the strong thermal interaction between them (Fig. 4a). In the tightly coupled method, sub-iterations are employed between coupled solvers at every CHT time step to maintain the continuity of thermal variables at the interface and achieve second-order temporal accuracy. The air solver was loosely coupled with the ice/conduction solvers (Fig. 4b), mainly due to the high computational cost of the air solver simulation. Under the loosely coupled approach, solvers exchange information only once per time step, necessitating a reduction in the coupling time step to mitigate numerical instabilities. It is worth mentioning that both couplings are based on a weak coupling method, which does not require complicated coupling of the water film between the air and solid domains.
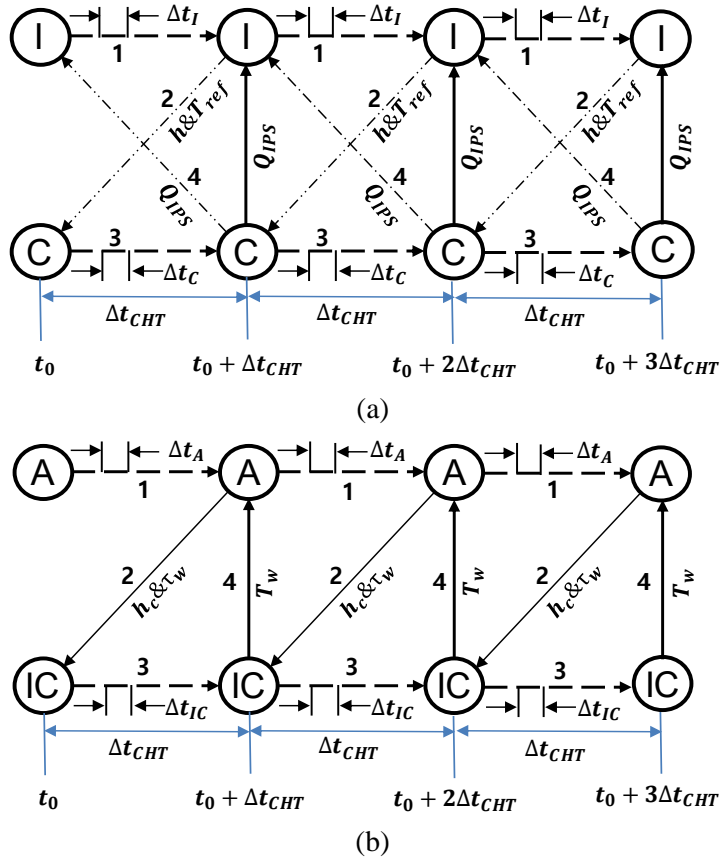
Fig. 4. Elaborate flowchart of (a) the tightly coupled approach for ice (I) and conduction (C) solvers and (b) the loosely coupled approach for air (A) and ice/conduction (IC) solvers.

In addition to the loose/tight coupling, the interface boundary conditions also affect the accuracy and stability of the coupling. In the icing community, the couplings of ice and conduction solvers are usually categorized as temperature-based and flux-based approaches [36, 50]. In the temperature-based approach, temperature distribution at the interface is calculated in the conduction solver and then transferred to the ice solver. In the ice solver, temperature is assumed to be a known quantity, and heat load is predicted using the heat balance in the ice/water layer. Heat load is applied as a Neumann boundary condition to the conduction solver to calculate the temperature distribution in the solid and on the wall. In this approach, the original PDE-based ice solver, based on the SWIM model, is modified such that melting occurs in an artificial temperature range near the melting temperature. The melting rate is calculated using the

18

unsteady freezing fraction by assuming a linear relation between the freezing fraction and temperature in the artificial temperature range [14].

Alternatively, the heat flux can be calculated in the conduction solver. Since heat flux is transferred to the ice solver, this is called the flux-based approach. In the ice solver, the temperature distribution of the ice and water layer is calculated based on the heat balance at the surface, which is transferred to the conduction solver as a Dirichlet BC. However, applying Dirichlet BC in the conduction solver can cause numerical stability issues [51]. As an alternative, we used an approach in which mixed BC was applied to the conduction solver.

A common approach to applying the mixed BC is to consider T_{ref} the free stream temperature and calculate the heat transfer coefficient, $h = Q/(T_{wall} - T_{ref})$. However, the heat transfer coefficient may become negative in regions where the heat flux's sign changes, resulting in an ill-posed heat conduction problem [27, 52]. Alternatively, a fixed predefined heat transfer coefficient is chosen to calculate the reference temperature as a function of the heat flux calculated in the conduction solver and the temperature calculated in the ice solver as follows [27]:

$$T_{ref} = T_{ice} - \frac{Q_{IPS}}{h},$$
(17)

where T_{ice} is the equilibrium temperature calculated in the ice solver, and Q_{IPS} is the heat flux calculated in the conduction solver. The value of h does not affect the final results. It only affects the convergence rate in sub-iterations of a CHT time step, knowing that the small values for h have a faster convergence but may result in numerical instability. As a result, the value of h (100 in this study) is a trade-off between the stability and computational time [27]. The reference temperature (T_{ref}) and heat transfer coefficient (h) are transferred to the conduction solver as a mixed boundary condition. Heat flux is calculated as a

function of the heat transfer coefficient, reference temperature, and temperature distribution calculated in the conduction solver (T_{cond}) as follows,

$$Q_{IPS} = h(T_{cond} - T_{ref}).$$

(18)

Overall, the temperature-based coupling requires very few iterations to converge for each coupling time step since temperature and heat flux continuity is always guaranteed at the interface. As a result, this approach provides a fast and robust simulation but requires very small CHT time steps. To avoid unphysical results, the coupling time step should be small enough to ensure that the change in surface temperature is not greater than the artificial phase temperature range. Otherwise, the ice solver can go directly from the rime region to the water film region without going through the glaze region. On the other hand, flux-based coupling with mixed BC provides more reliable results since it involves both solvers in the calculation of thermal variables at the interface. As a result, in this study, a flux-based approach with mixed BC for the conduction solver was used for all anti-icing simulations.

3. Numerical results of the electrothermal anti-icing simulation
3.1. Geometry and conditions

To evaluate the capabilities of the current anti-icing solver, we compared our numerical results with experimental data obtained in the NASA Lewis Icing Research Tunnel [22]. All experiments were performed over a rectangular wing with a NACA0012 section profile with a chord length equal to 0.9144m. The leading edge is a 6-layer composite that is equipped with seven heating pads implemented between composite layers. Fig. 5 represents the arrangement of heaters on the leading edge and the material compositions of the different composite layers. Heater A has a length of 19mm, Heaters B, C, D, and E are 25.4 mm wide, and finally, heaters F and G are 38.1 mm wide. During the manufacturing process, all of the heaters were shifted by 4.7625 mm toward the upper side of the airfoil [53]. The thickness and thermal properties of each layer of the leading edge are listed in Table 3.
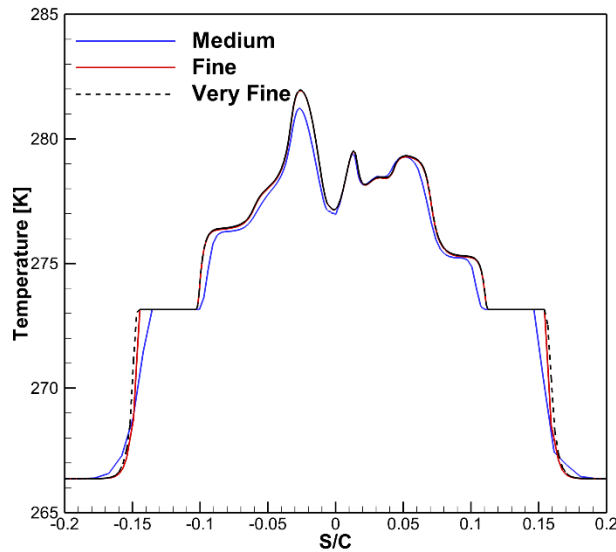
Table 3
Material properties of the composite layers.

Material	Thickness [mm]	ρ [kg/m^3]	k [W/m·K]	C_p [J/Kg·K]
Heating Element	0.013 (x1)	8906.3	41	385
Erosion Shield	0.203 (x1)	8025.3	16.3	502
Elastomer	0.280 (x2)	1383.9	0.256	1260
Fiberglass/Epoxy Composite	0.890 (x1)	1794.0	0.294	1570
Silicon Foam Insulation	3.430 (x1)	648.8	0.121	1130
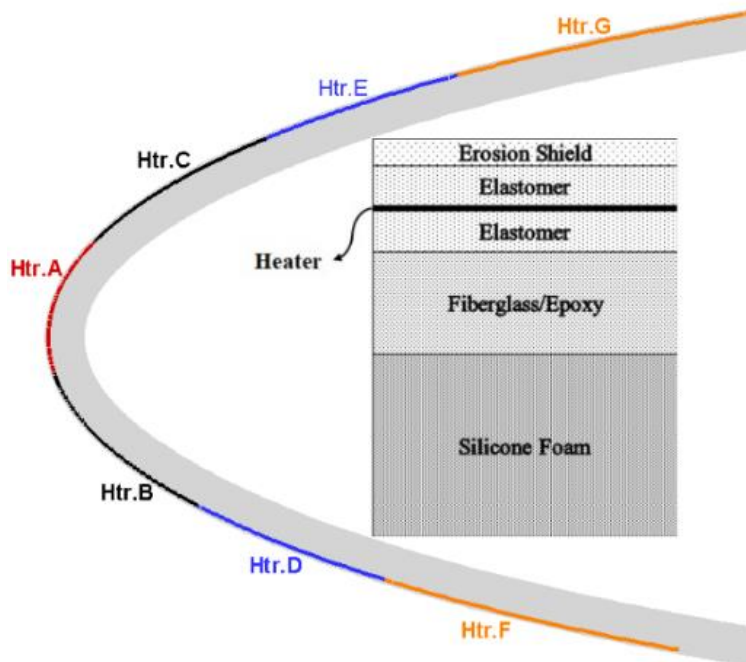
Fig. 5. Arrangement of heaters and cross-section of the leading edge.

Note that the same wing and IPS were used during the anti-icing and de-icing experiment campaign conducted at the NASA Lewis Icing Research Tunnel [22]. We conducted a mesh independence study using three grid sizes: medium (55,288/9,760 cells for air/solid domains), fine (121,473/18,920 cells for air/solid domains), and very fine (170,553/32,650 cells for air/solid domains). The wall temperature predictions for medium, fine, and very fine grids are plotted in Fig. 6. A far-field boundary condition was applied to the outer boundaries of the airflow domain. A Dirichlet-type inhomogeneous thermal boundary condition was also applied to the airfoil. The inner wall was assigned a zero heat flux boundary condition

within the solid domain, signifying negligible heat transfer through that surface. Conversely, the outer wall of the solid domain employs a conjugate heat transfer condition to capture the thermal interaction between the solid and the runback water film domain. The results showed that the results obtained by the fine grid almost match those of the very fine grid. As a result, we used the fine grid for the rest of the simulations. The only modification in the grid preparation was changing the height of the first cell based on the atmospheric conditions, to maintain the $y^+<1$. Among all the test cases provided in [22], four test cases were selected to validate the current solver. These test cases comprehensively cover all of the anti-icing regimes, including running wet, evaporative, and fully evaporative. The icing and atmospheric conditions of the validation test cases and their corresponding heater power densities are tabulated in Table 4.

Fig. 6. Comparison of temperature profiles for different grids for case 22B.

Table 4
Heater powers and icing conditions for the validation cases.

variables	Case 22B	Case 22A	Case 67B	Case 67A
Heater A [W/m^2]	4805	46500	15190	43400
Heater B [W/m^2]	4030	32550	10850	32550
Heater C [W/m^2]	2945	18600	9920	26350
Heater D [W/m^2]	2945	10230	11935	21700
Heater E [W/m^2]	3410	6975	12865	18600
Heater F [W/m^2]	2635	9920	8370	20150

Heater G [W/m^2]	2325	10230	8680	18600
T_∞ [K]	265.5	265.5	251.4	251.4
U_∞ [m/s]	44.7	44.7	89.4	89.4
LWC [g/m^3]	0.78	0.78	0.55	0.55
MVD [μm]	20	20	20	20

3.2. Verification of air/solid coupling through dry anti-icing simulations

The presence of runback water film on the surface makes the wet anti-icing simulation extremely complicated. As a result, anti-icing simulations were performed under dry air conditions to evaluate the coupling performance of the air solver in a relatively simpler scenario. The heater power densities and atmospheric conditions for case 22B were selected for dry anti-icing simulations. We did not consider supercooled water droplet impingement in these simulations, and only air and conduction solvers were coupled. The surface temperature distribution calculated in the conduction solver is transferred to the air solver as an inhomogeneous thermal BC. In the air solver, the heat transfer coefficient is updated based on the temperature profile obtained from the conduction solver. Subsequently, this updated heat transfer coefficient is transferred to the conduction solver as a convective boundary condition.

The air solver utilizes dual time-stepping in which a physical time step is used to march in time, and pseudo iterations (N_p) are utilized to converge the solution for each physical time step (Δt_A). The total number of iterations per time step is calculated by dividing the pseudo iterations over the air physical time step, as illustrated in Fig. 7a. The independence of the results to the total number of iterations per physical time step (Np/ΔtA) in the air solver was evaluated by conducting dry anti-icing simulations at four different N_p/Δt_A (100, 200, 500, and 1000 liter/s), which are plotted in Fig. 7b. The analysis of the results shows that temperature profiles corresponding to Np/ΔtA=500 iter/s match that of N_p/Δt_A=1000 iter/s, which enabled us to employ 500 iterations per second for the remaining simulations.

<center>(a)   (b)</center>
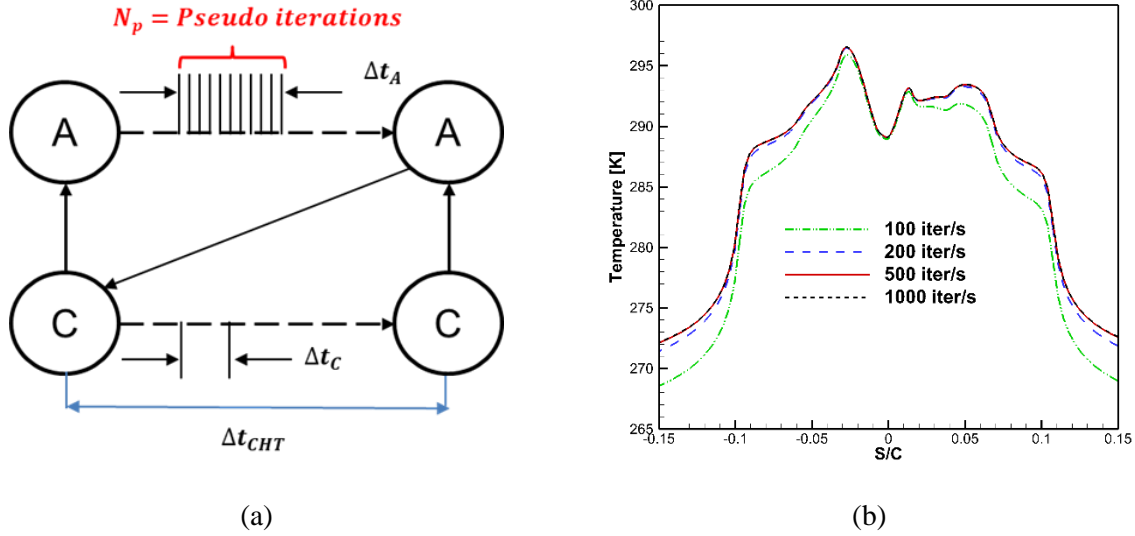
Fig. 7. (a) Illustration of Δt_{CHT}, air solver physical time step, and pseudo iterations and (b) Temperature profile for different $N_p/\Delta t_A$.

3.3. Validation of the electrothermal anti-icing solver

For the wet anti-icing simulations, four validation test cases were selected. For each case, a set of figures, including wall temperature, heat transfer coefficient, runback water film mass flow rate, and global heat transfer coefficient, were plotted and compared with the experimental data and numerical results wherever data was available. In addition, for all cases, anti-icing results obtained by the coupled solver and decoupled solver were compared together. In Messinger-based ice solvers, the water mass flow rate exiting the cell is calculated directly from the mass conservation equation by subtracting the ice accretion and evaporation rate from the water mass flow rate entering the cell. However, in the current PDE-based solver, the water flux for every cell is calculated using a roe scheme, which means that the exiting mass flow rate cannot be calculated directly in the simulation. Instead, we calculated the mass flow rate by defining mass flow rate as $\rho u A$ in which A equals the water film thickness multiplied by a constant number of one, and u is the mean water film velocity. The global heat transfer coefficient was calculated using the heat transfer coefficient, defined as follows,

<center>24</center>

$$h_{tot} = \frac{Q_{IPS}}{T_{wall} - T_{rec}}, \tag{19}$$

where Q_{IPS}, T_{wall}, and T_{rec} are the heat flux, temperature distribution at the wall, and recovery temperature. The definition of the global heat transfer coefficient, which was introduced by Al-Khalil [22], was not reported in their study. However, other studies [21, 30] have also used a similar definition, except that they used heater powers instead of heat flux at the wall.

3.3.1. Fully evaporative mode (case 22A)

Case 22A corresponds to a fully evaporative anti-icing regime since no water film exists beyond the impingement limits (Fig. 8b). The anti-icing temperature obtained by both the decoupled and coupled solvers match near the leading edge (Zones A, B, and C) since the CHTC in this region is not affected by thermal interaction from the wall [35] which is also illustrated in Fig. 8c. However, by moving toward the trailing edge (TE), the temperature prediction of the decoupled solver starts to deviate from that of the coupled solver and experimental data, where a dry surface is formed after impingement limits.

In the dry regions, there is no water to absorb heat from the surface. At the same time, the CHTC is low in regions far from LE, which increases temperature. The CHTC is not being updated by the temperature in the decoupled solver, causing an unphysical jump in wall temperature. On the other hand, in the coupled solvers, a change in wall temperature distribution affects CHTC, and a smooth increase in temperature is observed, which agrees with the experimental data. It is also worth mentioning that the anti-icing temperature obtained with the current coupled approach matches the experimental data.
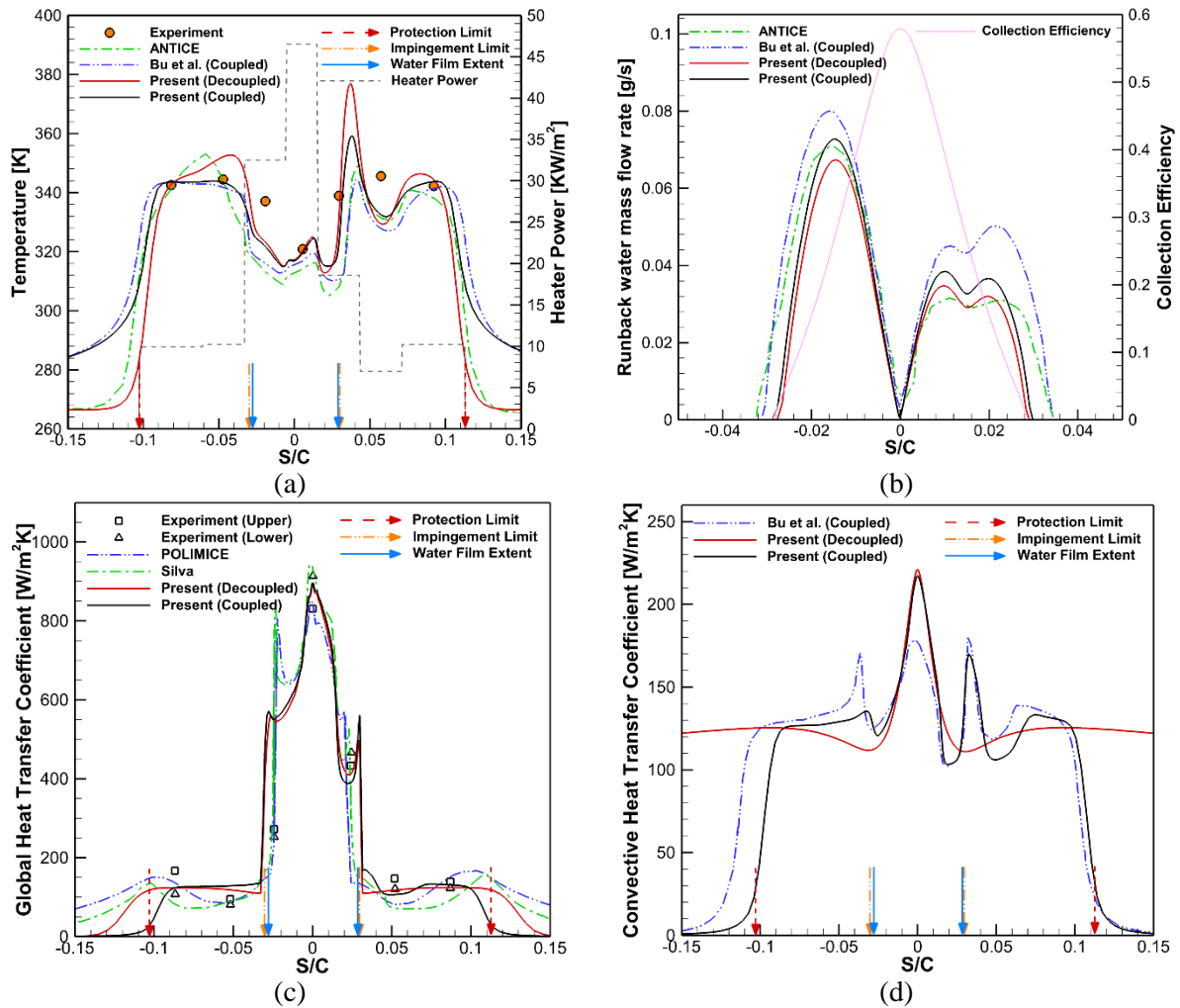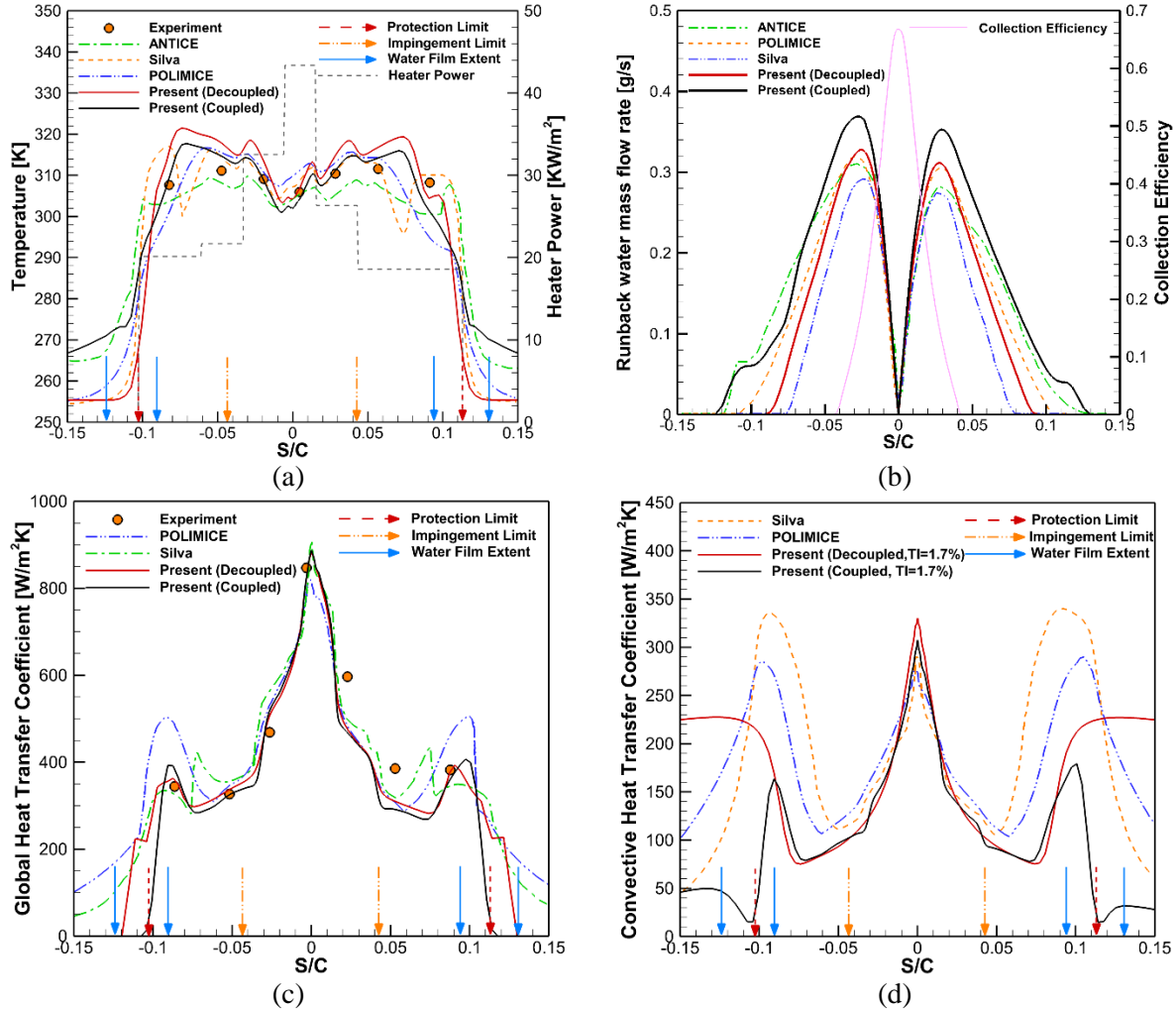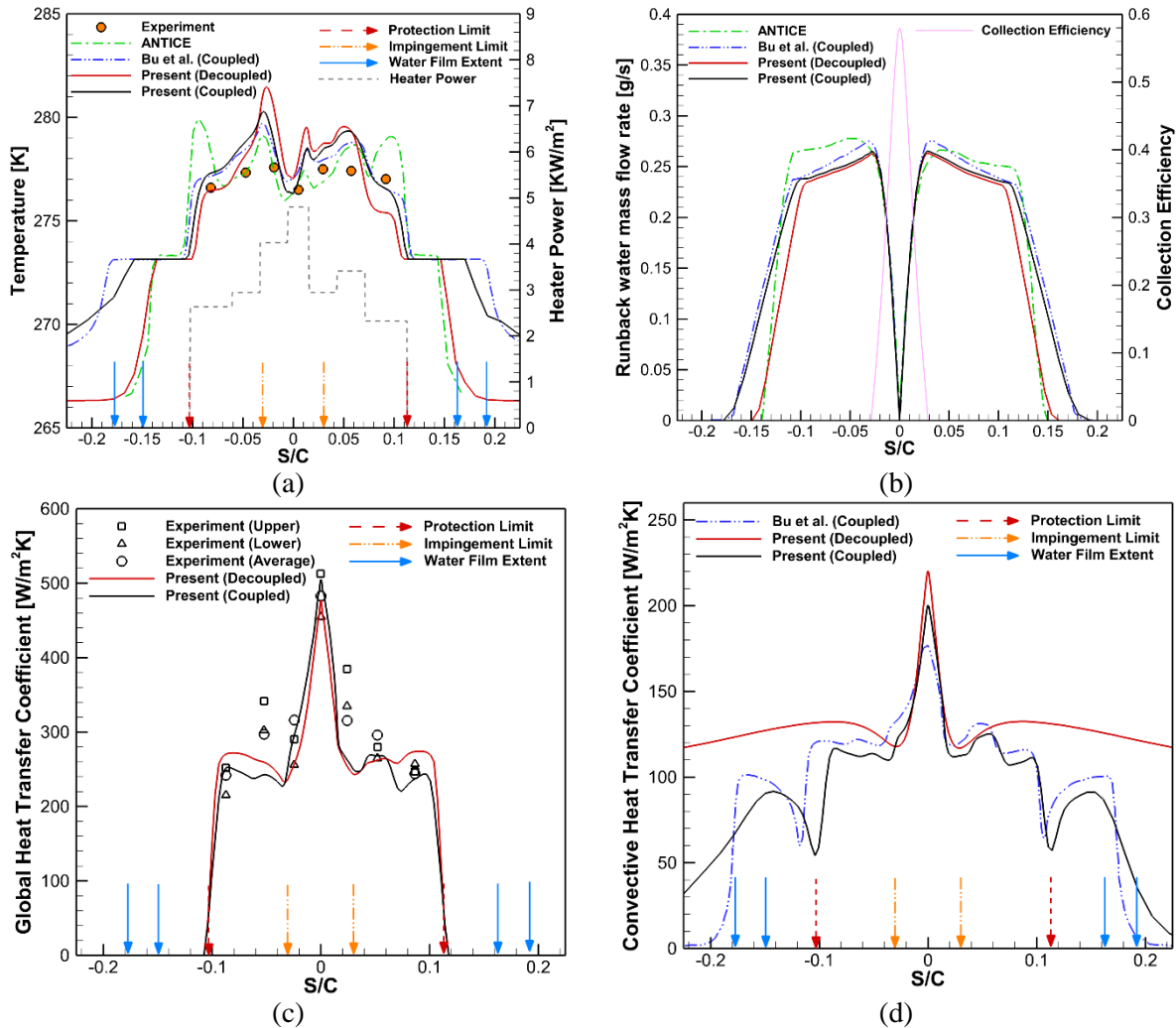
Fig. 8. Temperature profile (a), runback water mass flow rate (b), global heat transfer coefficient (c), and convective heat transfer coefficient (d) for anti-icing test case 22A.

3.3.2. Evaporative mode (case 67A)

Case 67A corresponds to the evaporative anti-icing regime since the runback water film exceeds the impingement limits but cannot flow beyond the protection limits due to evaporation. In this case, rivulets probably form at $S/C = \pm 0.07$. The formation of rivulets creates a partially dry surface, which affects the evaporation and heat balance on the surface. Moreover, it can facilitate the laminar boundary layer's transition to turbulence, significantly affecting CHTC. We did not consider the rivulet formation in the current numerical model. However, the effect of the transition on the CHTC is considered, which led to

good agreement between the current prediction of wall temperature and the experimental data (Fig. 9a).

The transition effect on CHTC can be seen in Fig. 9d.

Fig. 9. Temperature profile (a), runback water mass flow rate (b), global heat transfer coefficient (c), and convective heat transfer coefficient (d) for anti-icing test case 67A.

3.3.3. Running wet mode
A. Case 22B

For case 22B, the runback water flow accelerates rapidly inside the direct water droplet impingement area and, the mass flow rate of water film reduces due to evaporation in regions beyond the impingement limits (Fig. 10b). Once the runback water exceeds the protection limits, some portion of the water film freezes, which causes a sudden drop in the water mass flow rate (Fig. 10b). In this region, water and ice

coexist on the surface, corresponding to glaze ice accretion. In the glaze region, the temperature has a constant value of 273.15 K, which can be seen as the flat area in the temperature profile in Fig. 10a. The comparison of the decoupled and coupled solvers shows that the coupled solver predicts a wider flat area in the temperature profile. The temperature predictions of both the decoupled and coupled solvers match near the leading edge, as in case 22A. However, movement toward the TE at the upper side of the airfoil indicates there is a difference between the CHTC obtained by the coupled solver and the CHTC obtained by the homogeneous BC (Fig. 10d). This discrepancy in the CHTC results in the different temperature profiles predictions from the coupled and decoupled solvers.

Fig. 10. Temperature profile (a), runback water mass flow rate (b), global heat transfer coefficient (c), and convective heat transfer coefficient (d) for anti-icing test case 22B.

28

B. case 67B

Case 67B is classified as a running wet anti-icing regime since the runback water film exceeds the protection limits and an ice ridge forms on the surface. The temperature profile (Fig. 11a) obtained by the coupled solver is in better agreement with the experimental results than those from the decoupled solver. Results obtained by Silva [29] and POLIMICE [21], which are based on the integral boundary layer method, overpredicted the surface temperature for Regions A-E (an almost 10K difference can be seen in some locations) and underpredicted the temperature in regions F and G. This difference probably comes from the predicted location of the onset of transition in these models (Fig. 11d).
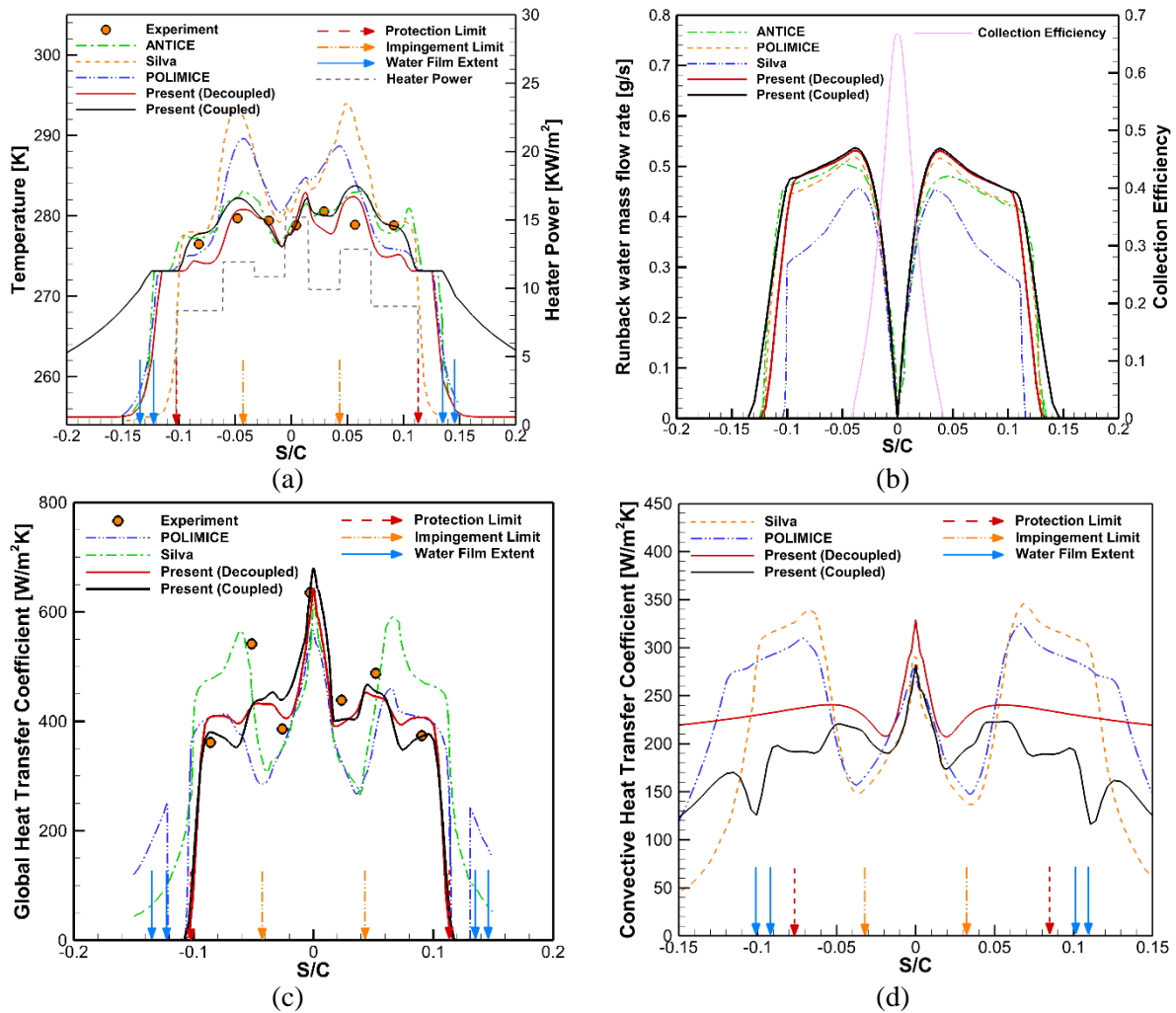
Fig. 11. Temperature profile (a), runback water mass flow rate (b), global heat transfer coefficient (c), and convective heat transfer coefficient (d) for anti-icing test case 67B.

4. Analysis of anti-icing results and discussions
4.1. Performance of new solver in comparison with experimental data and previous results

We computed the average temperature deviation of the solvers' predictions from experimental data by first calculating the deviations for each heater and then averaging them, summarized in Table 5. It should be mentioned that the wall temperature measurement from experiments is only available on 7 points (one for each heater). Analysis of the results revealed that the current coupled solver outperforms other solvers in nearly all scenarios. This is apparent in the fully evaporative mode (case 22A), where the temperature jump occurs in the protection limits. Here, the current coupled solver exhibited a 5.53 K absolute temperature deviation from experimental data, whereas the coupled solver of Bu et al. [35] showed a 10.76 K deviation, providing a significant 50% improvement.

Table 5
The average deviation of the solver's predictions from experimental data.

Solvers	Average Temperature Deviation from Experimental Data			
	Case 22A	Case 22B	Case 67A	Case 67B
ANTICE	11.27	0.85	3.93	1.45
Silva	-	-	2.56	5.55
PoliMIce	-	-	5.16	4.60
Bu et al. (Decoupled)	11.27	1.01	-	-
Bu et al. (Coupled)	10.76	0.81	-	-
Present (Decoupled)	7.10	1.42	4.88	1.91
Present (Coupled)	5.53	1.01	2.66	1.41

4.2. Effect of updating airflow on runback ice and wall temperature distribution

This section investigates the effect of updating airflow on the runback ice characteristics and wall temperature distribution under different icing and atmospheric conditions. For this purpose, six new cases were chosen from anti-icing experiments conducted at the NASA Lewis Icing Research Tunnel, as listed in Table 6. These test cases were chosen to cover different effective parameters like free stream temperature and velocity, LWC, and angle of attack.

Table 6

Heater powers and icing conditions for additional running wet cases.

variables	Case 48B	Case 58B	Case 65B	Case 71B	Case 87B	Case 91B
Heater A [W/m^2]	4960	9765	7595	5425	7130	9765
Heater B [W/m^2]	4030	7440	5890	4030	5425	6975
Heater C [W/m^2]	3565	5580	5580	2945	4030	6045
Heater D [W/m^2]	3100	6510	6200	3875	3875	7285
Heater E [W/m^2]	3565	6510	6820	3100	3875	5270
Heater F [W/m^2]	2635	5270	4805	3100	3410	6045
Heater G [W/m^2]	2635	4960	4495	3100	3100	5735
T_∞ [K]	265.5	254.4	262.5	265.5	262.7	254.4
U_∞ [m/s]	44.7	44.7	89.4	44.7	44.7	44.7
LWC [g/m^3]	1.1	1.1	0.55	0.78	2.0	0.78
MVD [µm]	20	20	20	20	20	20
Angle of attack	0	0	0	4	0	4

Runback ice can be characterized by three main factors: its maximum height (height), the location where ice formation begins (onset), and the length or extent of ice on the surface (extent). Among these, ice height is the most critical parameter, because it significantly affects and degrades aerodynamic performance. The shape of the runback ice depends on the icing conditions and the power densities of the heaters used. To maintain consistency in the approach to heater powers, their values were chosen based on experimental data. A comprehensive analysis was conducted by performing quantitative evaluations and qualitative comparisons. This analysis aimed to study the impact of updating the airflow field on anti-icing results.

To achieve this goal, wall temperature distribution (for all cases) and runback ice characteristics (for running wet anti-icing mode) were calculated using coupled and decoupled solvers. Subsequently, deviations between the results obtained from the decoupled solvers and coupled solvers were calculated as a percentage of deviation. Runback ice characteristics (Runback ice height, onset location, ice length) and temperature deviation norms are summarized in Table 7. Table 7 quantifies the effects of updating airflow on anti-icing results in terms of deviations of coupled and decoupled solvers in wall temperature and runback ice shape. The L∞-norm, L1-norm, and L2-norm represent the maximum deviation, the average deviation over all the cells, and the Euclidean norm, respectively.

Table 7
Wall temperature and runback ice shape deviations of coupled and decoupled solvers for different anti-icing cases.

Case	Runback ice characteristics						Wall temperature		
	Upper side			Lower side			L1-	L2-	L∞-
	Height	Onset	Extent	Height	Onset	Extent	norm	norm	norm
Case 22A	-	-	-	-	-	-	3.40	6.65	26.47
Case 22B	40.2%	3.3%	48.8%	38.8%	3.3%	46.6%	0.65	1.00	4.97
Case 48B	37.9%	6.4%	47.2%	33.4%	3.6%	47.0%	0.38	0.74	4.58
Case 58B	23.8%	0.1%	35.3%	25.4%	0.0%	33.8%	0.70	1.71	11.41
Case 65B	66.0%	6.7%	64.0%	62.7%	3.1%	69.1%	1.71	2.17	6.67
Case 67A	-	-	-	-	-	-	3.01	4.54	18.59
Case 67B	42.1%	3.4%	24.6%	35.4%	3.5%	23.4%	1.32	2.74	13.81
Case 71B	38.5%	3.1%	28.7%	49.8%	6.3%	70.4%	0.54	0.97	4.76
Case 87B	23.5%	0.3%	33.8%	24.5%	3.4%	29.4%	0.35	0.73	6.14
Case 91B	43.0%	7.0%	78.9%	53.7%	9.5%	57.1%	1.12	2.66	16.21

4.2.1. Analysis of the deviations in wall temperature distribution

The CHTC remains relatively unchanged when the isothermal wall temperature is altered. However, variations in the surface temperature distribution can significantly impact the heat transfer coefficient. When surface temperature increases, the temperature in the boundary layer of airflow also increases. As a result, the CHTC does not change significantly in the case of isothermal wall temperature. However, if surface temperature changes in the streamwise direction, the colder airflow that reaches the hot area increases the cooling capacity of the airflow, increasing the CHTC [35]. Consequently, the wall temperature distribution obtained from the decoupled solver deviates from the coupled solver in regions that have a considerable temperature gradient on the surface. This is because when a sudden temperature change occurs, the heat transfer characteristics of the boundary layer change, resulting in a difference in the heat transfer coefficient.

Since the decoupled solver does not update the heat transfer coefficient, it predicts an unphysical temperature in these regions. For example, in Fig. 8a (temperature profile for case 22A), two types of temperature jumps are visible: first at the boundary of the dry/wet region (in case 22A, droplet impingement limits at $S/C = \pm 0.03$) and second at the protection limits. In both cases, the surface temperature predicted by the decoupled solver deviates from the coupled solver (Table 7). The water film

32

reaches the protection limits in the running wet anti-icing mode, leading to temperature jumps that occur solely at these limits. In the evaporative mode, where dry regions form within these protection limits, deviations in temperature between the decoupled and coupled solvers are notably more significant. This phenomenon is supported by the wall temperature data presented in Table 7. Specifically, the error norms of wall temperature in evaporative modes (case 22A and case 67A) stand out, and are the highest among all cases.

The common practice in the design of electrothermal ice protection systems is to adjust the heater powers such that the surface reaches a target wall temperature. This target wall temperature for running wet and evaporative systems can be set to 277-278 K and 310-320 K [22]. Because there are errors in the numerical predictions of anti-icing wall temperature, safety factors must be considered in the design process. Increasing the accuracy of numerical predictions can reduce these safety factors, ultimately saving energy. Decoupled solvers can be used to design running wet anti-icing regimes where a target wall temperature strategy is employed. The reason is that the deviation between coupled and decoupled solvers in running wet regimes is insignificant. However, for evaporative cases, the mean error of wall temperature distribution between the coupled and decoupled solvers is 3.4 K and 3.0 K for case 22A and case 67A, respectively (Table 7). As a result, using the decoupled solvers for evaporative anti-icing regimes can increase uncertainty in heat load calculation.

We calculated the required heat load for various target wall temperatures of a wing with a span of 1 meter for case 22, which is shown in Fig. 12. This analysis shows that the 1 K temperature difference results in an almost 40 W difference in heat load calculation at the target wall temperature of 274K. The difference reaches almost 77 W for a target wall temperature of 290K.
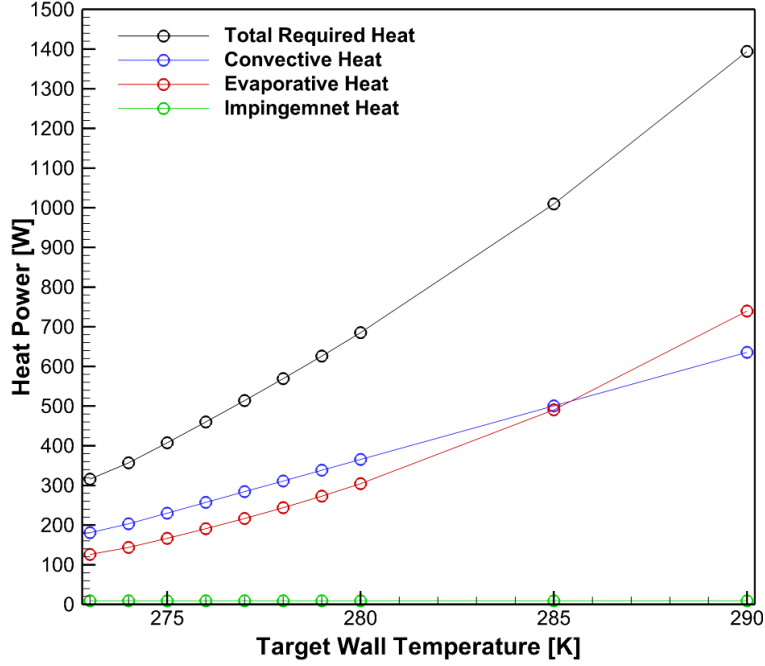
**Fig. 12.** Total heat required at different target wall temperatures.

Next, correlation coefficients were calculated to determine the correlations between the input parameters (LWC, U_∞, T_{tot}, and total heat power) and output parameters (L1-norm, L2-norm, and L∞-norm). For this purpose, we used the Pearson correlation coefficient which can be calculated as follows,

$$ r = \frac{\sum (X_i - \bar{X})(Y_i - \bar{Y})}{\sqrt{\sum (X_i - \bar{X})^2 \sum (Y_i - \bar{Y})^2}} \tag{20}$$

where X_i and Y_i are the individual data points, and $\bar{X}$ and $\bar{Y}$ are the means of the variables. Variable r is the correlation coefficient which can have values between -1 to +1. Positive (negative) values of r show that if the first variable increases, the value of the other variable also increases (decreases).

Figure 13 illustrates the correlation coefficients between icing conditions and absolute deviations of temperature predictions obtained by coupled and decoupled solvers. Total heat power correlated highest with temperature deviation norms since higher power heat densities result in evaporative mode at the same icing conditions (Fig. 13a). Lower LWCs and higher velocities correlate higher with average

34

temperature deviations (L1-norm). In other words, the highest temperature deviation for the running wet cases was observed in cases 65B and 67B, which have the highest velocities and lowest LWC among other cases. The total temperature was most highly correlated with the L∞-norm, which means that cases with the lowest total temperatures (58B, 67B, and 91B) have the highest temperature deviation.

(a) Total heat power

(b) LWC

(C) Free stream velocity

(d) Total temperature
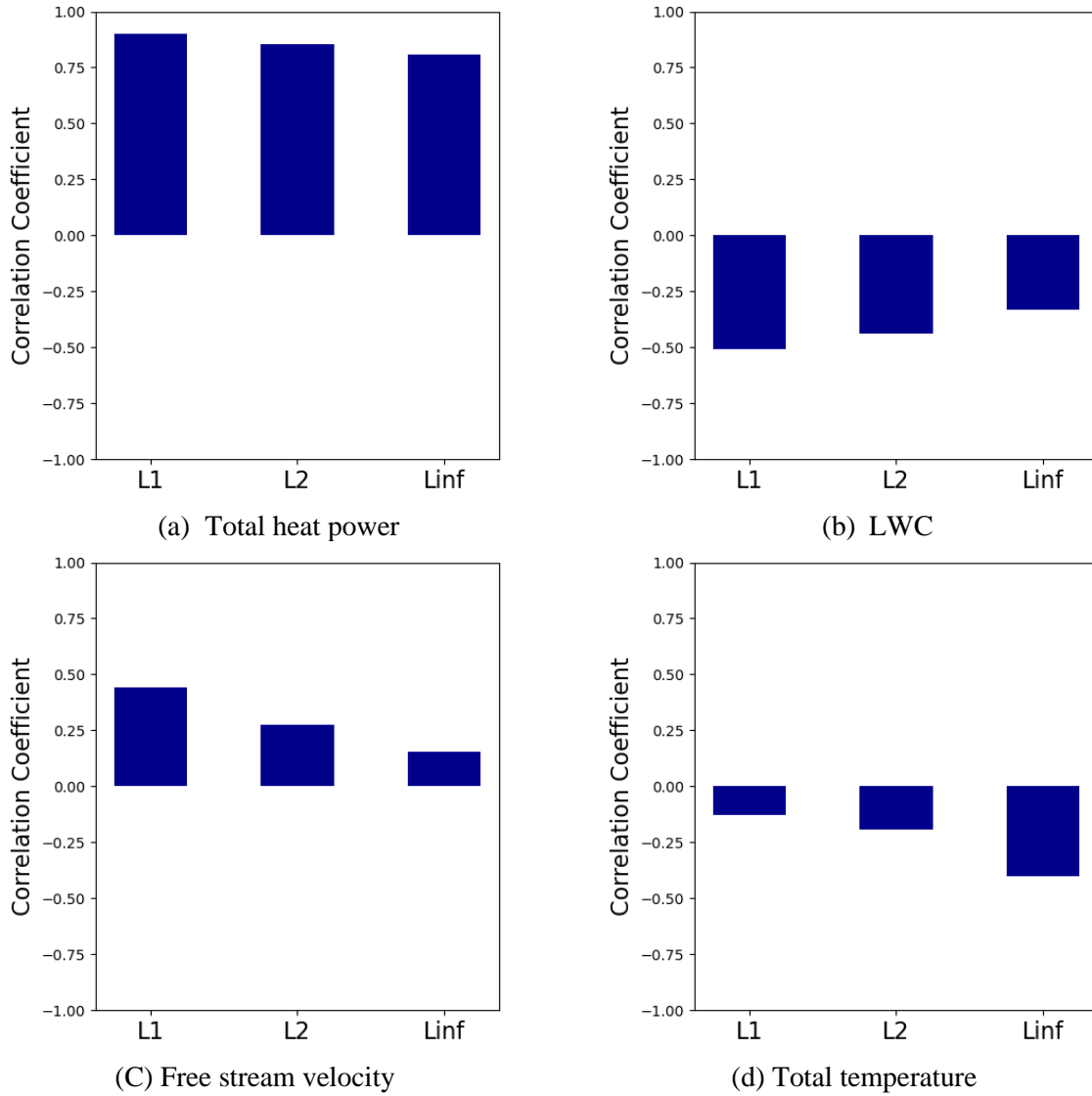
Fig. 13. Bar charts for correlation coefficients between input parameters and absolute temperature deviations of coupled and decoupled solvers.

4.2.2.Analysis of deviations in the shape of runback ice

In the running wet anti-icing regime, the runback water film exceeds the protection limits, and an ice ridge forms in unprotected areas. However, the coupled and decoupled solvers predict significantly different ice shapes, as summarized in Figs. A1 to A8 of Appendix A. The decoupled solver predicts thicker ice with a narrower ice extent on the surface, while the coupled solver estimates thinner ice with a broader extent. The reason is that in the decoupled solver, the temperature drops abruptly out of protection limits, which means that a considerable portion of the water film freezes in the glaze region. On the other hand, the coupled solver predicts higher temperatures in unprotected areas, which results in lower ice accretion rates. Since the water mass on the surface is conserved, the water film can flow further in the coupled solver, resulting in a wider ice extent on the surface. This difference in the predictions of runback ice obtained by the coupled and decoupled solvers can be seen in all cases.

Figure 14 shows correlation coefficients between icing conditions and geometrical characteristics of runback ice shape. LWC and Free stream velocity have the highest impact on deviations of maximum runback ice height according to the results obtained by the coupled and decoupled solvers. For example, the maximum ice height had maximum deviations for case 65B (66% and 63% for the upper and lower side, respectively), which had the highest velocity and lowest LWC among all cases (compare Fig. A4a and A4b). On the other hand, total temperature and angle of attack had the highest positive correlation with deviations in runback ice extent. In other words, for cases with higher total temperature and higher angle of attack, like case 71B, the deviation in runback ice extent reached its maximum (compare the lower side ice in Figs. A7a and A7b). Finally, the angle of attack and LWC had the highest impact on deviations in the onset location of runback ice on the lower and upper surface of the airfoil, respectively. For example, in case 91B, the deviation in the onset location of ice accretion between coupled and decoupled solvers reached 9.5% (compare Figs. A8a and A8b).

Runback ice formation in the running wet regimes can disrupt the airflow on the wing, which may increase drag and decrease the lift. As a result, considering the effect of runback ice shape on aerodynamic performance can help optimize the heat power densities in running wet regimes. Extending the protection limits is a common practice to avoid aerodynamic performance degradation in running wet regimes. The results show that the decoupled solvers overpredict the runback ice shape in unprotected areas. As a result, extending the protection limits based on the runback ice shapes predicted by decoupled solvers can unnecessarily increase the total heat power.

(a) Total temperature

(b) LWC

(c) Free stream velocity

(d) Angle of attack
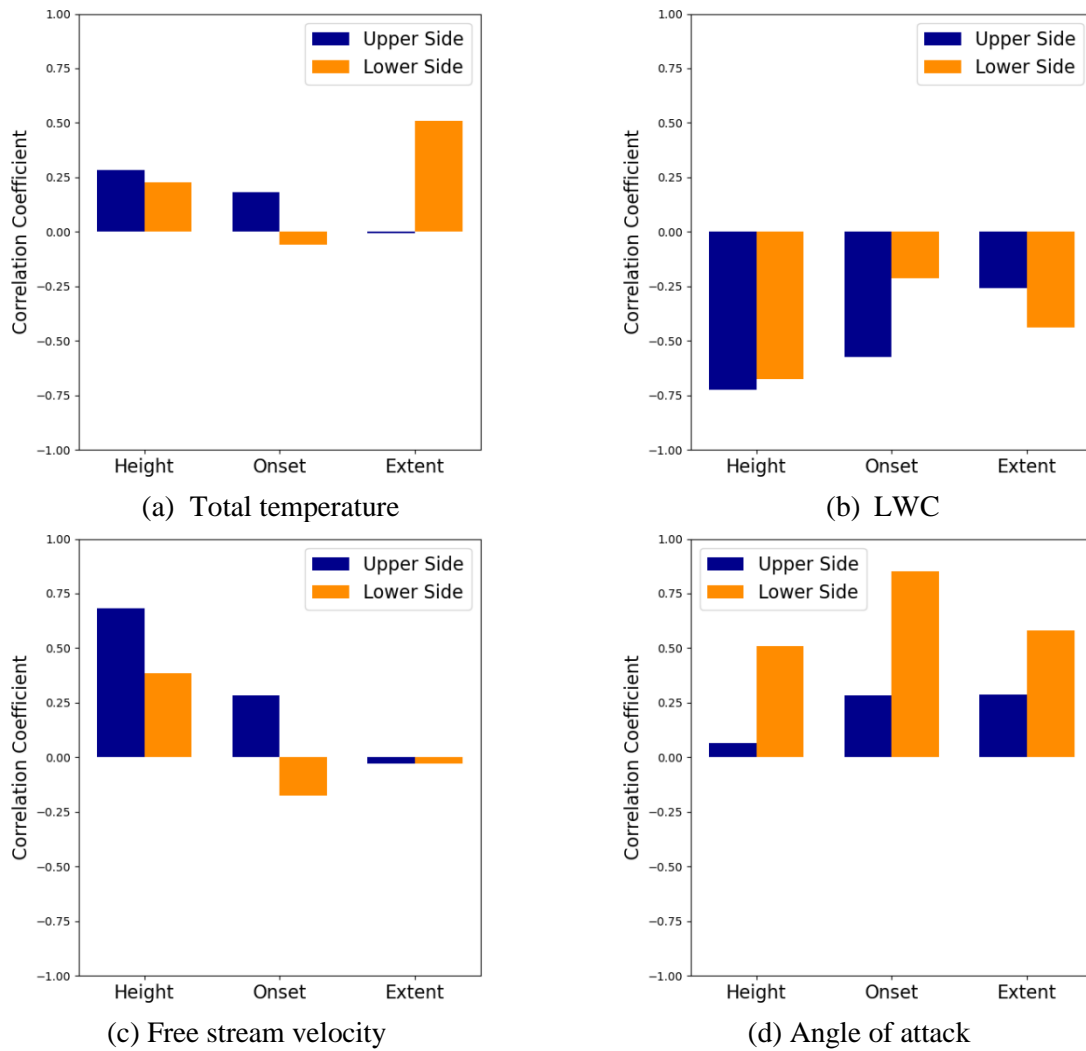
Fig. 14. Bar charts showing correlation coefficients between icing conditions and runback ice shape characteristics.

5. Conclusions

A novel approach for updating airflow in anti-icing simulation was developed. The current approach employs an inhomogeneous thermal boundary condition to update the convective heat transfer coefficient based on the transient wall temperature distribution. A unified finite volume framework consisting of a compressible Navier-Stokes-Fourier airflow solver, a Eulerian droplet impingement solver, an unsteady PDE-based ice accretion/melting solver, and a multilayer heat conduction solver was developed to simulate electrothermal anti-icing processes. Thermal interaction between the different solvers was modeled using the conjugate heat transfer method. A flux-based approach was utilized to couple the ice and conduction solver, which directly calculates the surface temperature in the ice solver without the need for further assumptions for phase change temperature. A mixed boundary condition was applied to the conduction solver to engage ice and conduction solvers in calculating interface thermal variables. In contrast to the common approach, the heat transfer coefficient was chosen as a fixed and predefined variable to avoid negative heat transfer coefficient values. Instead, the reference temperature was calculated based on the ice solver's temperature distribution and the conduction solver's heat flux.

In addition, we investigated the effect of updating the air flow field, and particularly the convective heat transfer coefficient, on the anti-icing results. For this purpose, two distinct solvers, a coupled and a decoupled solver, were developed. In the decoupled solver, the convective heat transfer coefficient is obtained using the homogeneous thermal boundary condition and remains unchanged during the anti-icing simulation. In the coupled solver, the temperature distribution calculated in the ice/conduction solver is used in the air solver as an inhomogeneous thermal boundary condition to update the convective heat transfer coefficient. Four validation test cases corresponding to the different anti-icing regimes, including fully evaporative, evaporative, and running wet mode, were chosen to validate the current solver with experimental data. For each case, temperature distribution, convective heat transfer coefficient, global heat transfer coefficient, and runback water mass flow rate profiles obtained by the current coupled

and decoupled solver were compared. Analysis of average temperature deviations from experimental data showed that the present solver performs better in predicting wall temperature, especially in evaporative anti-icing regimes.

Wall temperature predictions of decoupled solver have the highest deviation from that of coupled solver where sudden jumps occur in surface temperature. The highest deviations were observed in evaporative mode cases, where dry regions form within the protection limits. Our analysis shows that decoupled solvers can be used to design running wet anti-icing regimes where a target wall temperature strategy is employed. Moreover, using coupled solvers for designing ice protection systems in evaporative anti-icing regimes improves temperature prediction accuracy, which enables the designers to reduce the safety factors and save energy. Moreover, the height, onset location, and extent of runback ice predicted by the decoupled solver deviated significantly from the coupled solver predictions. The coupled solver predicts thinner but wider runback ice, while the decoupled solver estimates a thicker and narrower ice ridge. The maximum deviation in ice height was observed for cases with the highest free stream velocity and lowest LWC.

We note that solving the Navier-Stokes equations for each airflow update is computationally expensive compared to low-fidelity solvers like the panel method. We employed two strategies to speed up the simulations and increase the efficiency: Parallelization of the airflow solver using the MPI method and a dual time-stepping approach with larger physical time steps. Furthermore, the present PDE-based ice solver assumes that the runback water film fully wets the surface. However, experimental observations show that the water film may split into rivulets or isolated beads when it flows beyond the impingement limits. The formation of dry patches can affect the surface's heat balance and the laminar to turbulent transition, altering the convective heat transfer coefficient. As a result, developing a numerical model to predict the rivulet formation and wetness factor may be considered as a future study.

Acknowledgment

References

[1] Y. Cao, W. Tan, Z. Wu, Aircraft icing: An ongoing threat to aviation safety, Aerosp. Sci. Technol. 75 (2018) 353-385.

[2] Y. Cao, Z. Wu, Y. Su, Z. Xu, Aircraft flight characteristics in icing conditions, Prog. Aerosp. Sci. 74 (2015) 62-80.

[3] R.W. Gent, N.P. Dart, J.T. Cansdale, Aircraft icing, Philos. Trans. R. Soc. London, Ser. A 358 (2000) 2873-2911.

[4] Y.M. Lee, J.H. Lee, L.P. Raj, J.H. Jo, R.S. Myong, Large-eddy simulations of complex aerodynamic flows over multi-element iced airfoils, Aerosp. Sci. Technol. 109 (2021) 106417.

[5] L. Prince Raj, E. Esmaeilifar, H. Jeong, R.S. Myong, Computational simulation of glaze ice accretion on a rotorcraft engine intake in large supercooled droplet icing conditions, AIAA Paper 2022-0447, AIAA SciTech 2022 Forum, 2022.

[6] L.P. Raj, K. Yee, R.S. Myong, Sensitivity of ice accretion and aerodynamic performance degradation to critical physical and modeling parameters affecting airfoil icing, Aerosp. Sci. Technol. 98 (2020) 105659.

[7] L.P. Raj, J. Lee, R.S. Myong, Ice accretion and aerodynamic effects on a multi-element airfoil under SLD icing conditions, Aerosp. Sci. Technol. 85 (2019) 320-333.

[8] L.P. Raj, High-Fidelity Computational Modeling of In-Flight Ice Accretion on Aircraft and Rotorcraft Including Super cooled Large Droplet, Ph. D. Thesis, Gyeongsang National University, 2017.

[9] S. Min, K. Yee, Numerical investigation of the unsteady effect owing to oscillation on airfoil icing, Int. J. Heat Mass Transfer 203 (2023) 123791.

[10] B. Sengupta, L.P. Raj, M. Cho, C. Son, T. Yoon, K. Yee, R.S. Myong, Computational simulation of ice accretion and shedding trajectory of a rotorcraft in forward flight with strong rotor wakes, Aerosp. Sci. Technol. 119 (2021) 107140.

[11] A. Lampton, J. Valasek, Prediction of icing effects on the lateral/directional stability and control of light airplanes, Aerosp. Sci. Technol. 23 (2012) 305-311.

[12] T.P. Ratvasky, B.P. Barnhart, S. Lee, Current methods modeling and simulating icing effects on aircraft performance, stability, control, J. Aircr. 47 (2010) 201-211.

[13] A. Rabiei Beheshti, Y.S. Kim, R.S. Myong, Adaptive Robust Servo LQR control of aircraft in icing condition, AIAA Paper 2023-1636, AIAA SciTech 2023 Forum, 2023.

[14] E. Esmaeilifar, L.P. Raj, R.S. Myong, Computational simulation of aircraft electrothermal de-icing using an unsteady formulation of phase change and runback water in a unified framework, Aerosp. Sci. Technol. 130 (2022) 107936.

[15] S. Jung, L.P. Raj, A. Rahimi, H. Jeong, R.S. Myong, Performance evaluation of electrothermal anti-icing systems for a rotorcraft engine air intake using a meta model, Aerosp. Sci. Technol. 106 (2020) 106174.

[16] R. Roy, L.P. Raj, J.H. Jo, M.Y. Cho, J.H. Kweon, R.S. Myong, Multiphysics anti-icing simulation of a CFRP composite wing structure embedded with thin etched-foil electrothermal heating films in glaze ice conditions, Compos. Struct. 276 (2021) 114441.

[17] J.-S. Lee, H. Jo, H.-S. Choe, D.-S. Lee, H. Jeong, H.-R. Lee, J.-H. Kweon, H. Lee, R.S. Myong, Y. Nam, Electro-thermal heating element with a nickel-plated carbon fabric for the leading edge of a wing-shaped composite application, Compos. Struct. 289 (2022) 115510.

[18] S.K. Thomas, R.P. Cassoni, C.D. MacArthur, Aircraft anti-icing and de-icing techniques and modeling, J. Aircr. 33 (1996) 841-854.

[19] X. Huang, N. Tepylo, V. Pommier-Budinger, M. Budinger, E. Bonaccurso, P. Villedieu, L. Bennani, A survey of icephobic coatings and their potential use in a hybrid coating/active ice protection system for aerospace applications, Prog. Aerosp. Sci. 105 (2019) 74-97.

[20] G.A.L. da Silva, O. de Mattos Silvares, E.J.G. de Jesus Zerbini, Numerical simulation of airfoil thermal anti-ice operation, part 1: mathematical modelling, J. Aircr. 44 (2007) 627-633.

[21] B.A. Gutiérrez, A. Della Noce, M. Gallia, T. Bellosta, A. Guardone, Numerical simulation of a thermal Ice Protection System including state-of-the-art liquid film model, J. Comput. Appl. Math. 391 (2021) 113454.

[22] K. Al-Khalil, C. Horvath, D. Miller, W. Wright, K. Al-Khalil, C. Horvath, D. Miller, W. Wright, Validation of NASA thermal ice protection computer codes. III-The validation of ANTICE, AIAA Paper 97-0051, 35th Aerospace Sciences Meeting and Exhibit, 1997.

[23] B. Arizmendi Gutiérrez, A. Della Noce, M. Gallia, A. Guardone, Optimization of a Thermal Ice Protection System by means of a genetic algorithm, in: International Conference on Bioinspired Methods and Their Applications, Springer, 2020.

[24] M. Gallia, B. Arizmendi Gutiérrez, G. Gori, A. Guardone, P.M. Congedo, Robust Optimization of a Thermal Anti-Ice Protection System in Uncertain Cloud Conditions, J. Aircr. (2023) 1-15.

[25] M. Pourbagian, W.G. Habashi, Aero-thermal optimization of in-flight electro-thermal ice protection systems in transient de-icing mode, Int. J. Heat Fluid Flow 54 (2015) 167-182.

[26] M. Pourbagian, W.G. Habashi, Surrogate-based optimization of electrothermal wing anti-icing systems, J. Aircr. 50 (2013) 1555-1563.

[27] T. Verstraete, S. Scholl, Stability analysis of partitioned methods for predicting conjugate heat transfer, Int. J. Heat Mass Transfer 101 (2016) 852-869.

[28] B. John, P. Senthilkumar, S. Sadasivan, Applied and theoretical aspects of conjugate heat transfer analysis: a review, Arch. Comput. Methods Eng. 26 (2019) 475-489.

[29] G. Silva, O. Silvares, E. Zerbini, H. Hefazi, H.-H. Chen, K. Kaups, Differential boundary-layer analysis and runback water flow model applied to flow around airfoils with thermal anti-ice, AIAA Paper 2009-3967, 1st AIAA Atmospheric and Space Environments Conference, 2009.

[30] G.A.L.d. Silva, O.d.M. Silvares, E.J.d.G.J. Zerbini, Numerical simulation of airfoil thermal anti-ice operation, part 2: implementation and results, J. Aircr. 44 (2007) 634-641.

[31] K.M. Al-Khalil, Numerical Simulation of an Aircraft Anti-icing System Incorporating a Rivulet Model for the Runback Water, Ph. D. Thesis, The University of Toledo, 1991.

[32] K.M. Al-Khalil, T.G. Keith Jr, K.J. De Witt, Development of an improved model for runback water on aircraft surfaces, J. Aircr. 31 (1994) 271-278.

[33] F. Morency, F. Tezok, I. Paraschivoiu, Heat and mass transfer in the case of anti-icing system simulation, J. Aircr. 37 (2000) 245-252.

[34] K.M. Al-Khalil, T.G. Keith Jr, K.J. De Witt, Further development of an anti-icing runback model, AIAA Paper 91-0266, 29th Aerospace Sciences Meeting, 1991.

[35] X. Bu, G. Lin, X. Shen, Z. Hu, D. Wen, Numerical simulation of aircraft thermal anti-icing system based on a tight-coupling method, Int. J. Heat Mass Transfer 148 (2020) 119061.

[36] X. Shen, Q. Guo, G. Lin, Y. Zeng, Z. Hu, Study on loose-coupling methods for aircraft thermal anti-Icing system, Energies 13 (2020) 1463.

[37] Y. Bourgault, W.G. Habashi, J. Dompierre, G.S. Baruzzi, A finite element method study of Eulerian droplets impingement models, Int. J. Numer. Methods Fluids 29 (1999) 429-449.

[38] S.K. Jung, R.S. Myong, A second-order positivity-preserving finite volume upwind scheme for air-mixed droplet flow in atmospheric icing, Comput. Fluids 86 (2013) 459-469.

[39] Y. Kim, Y. Hong, S. Shon, K. Yee, Implementation of the DADI method into the droplet equation for efficient aircraft icing simulation, SAE Technical Paper 0148-7191, 2023.

[40] Y. Bourgault, H. Beaugendre, W.G. Habashi, Development of a shallow-water icing model in FENSAP-ICE, J. Aircr. 37 (2000) 640-646.

[41] L.P. Raj, E. Esmaeilifar, B. Sengupta, H. Jeong, R. Myong, Coarray Fortran parallel implementation of a finite volume method-based aircraft ice accretion simulation code, Int. J. Aeronaut. Space Sci. (2023) 1-12.

[42] A. Jameson, Time dependent calculations using multigrid, with applications to unsteady flows past airfoils and wings, AIAA Paper 91-1596, 10th Computational Fluid Dynamics Conference, 1991.

[43] J. Blazek, Computational Fluid Dynamics: Principles and Applications, Butterworth-Heinemann, 2015.

[44] S.C. Cakmakcioglu, O. Bas, U. Kaynak, A correlation-based algebraic transition model, Proc. Inst. Mech. Eng., Part C: J. Mech. Eng. Sci. 232 (2018) 3915-3929.

[45] S.C. Cakmakcioglu, O. Bas, R. Mura, U. Kaynak, A revised one-equation transitional model for external aerodynamics, AIAA Paper 2020-2706, AIAA Aviation 2020 Forum, 2020.

[46] R. Mura, S.C. Cakmakcioglu, A revised one-equation transitional model for external aerodynamics-part i: Theory, validation and base cases, AIAA Paper 2020-2714, AIAA Aviation 2020 Forum, 2020.

[47] B. Aupoix, P. Spalart, Extensions of the Spalart–Allmaras turbulence model to account for wall roughness, Int. J. Heat Fluid Flow 24 (2003) 454-462.

[48] G.B. Schubauer, P.S. Klebanoff, Contributions on the mechanics of boundary-layer transition, 1956.

[49] R.K. Jeck, Icing Design Envelopes (14 CFR Parts 25 and 29, Appendix C) Converted to a Distance-Based, Federal Aviation Administration, US Department of Transportation: Washington, DC, USA (2002).

[50] X. Shen, H. Wang, G. Lin, X. Bu, D. Wen, Unsteady simulation of aircraft electro-thermal deicing process with temperature-based method, Proc. Inst. Mech. Eng., Part G: J. Aerosp. Eng. 234 (2020) 388-400.

[51] H.Z. Wang, 3D conjugate heat transfer simulation of aircraft hot-air anti-icing systems, Ph. D. Thesis, McGill University, 2005.

[52] A. Montenay, L. Paté, J. Duboué, Conjugate heat transfer analysis of an engine internal cavity, Turbo Expo: Power for Land, Sea, and Air, American Society of Mechanical Engineers, 2000.

[53] D. Miller, T. Bond, D. Sheldon, W. Wright, T. Langhals, K. Al-Khalil, H. Broughton, D. Miller, T. Bond, D. Sheldon, Validation of NASA thermal ice protection computer codes. I-program overview, AIAA Paper 97-0049, 35th Aerospace Sciences Meeting and Exhibit, 1997.

Appendix A

Figures A1 to A8 illustrate the runback ice and water film on the wing along with the temperature contour in the leading edge for the running wet mode cases listed in Table 4 and Table 6.
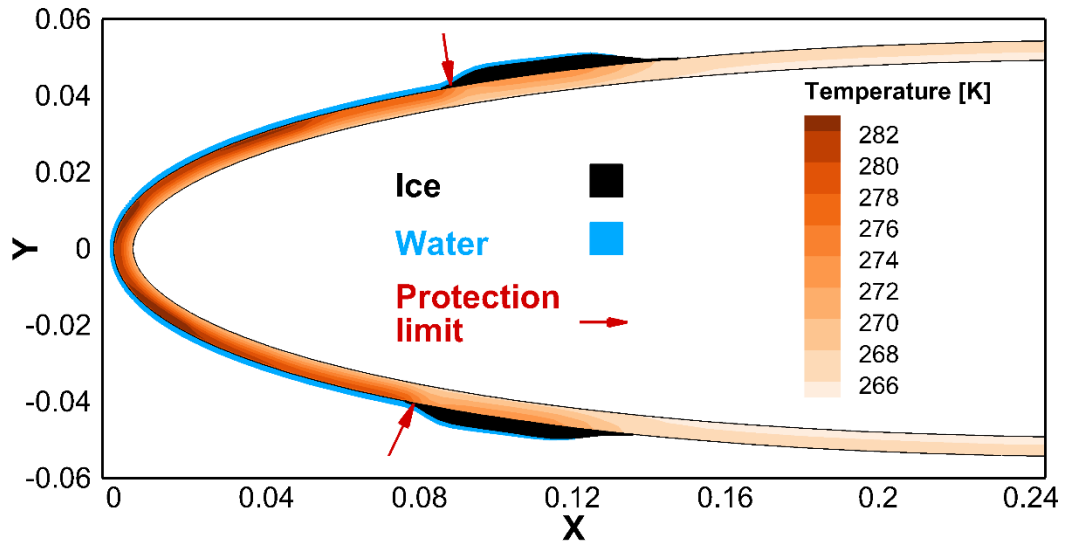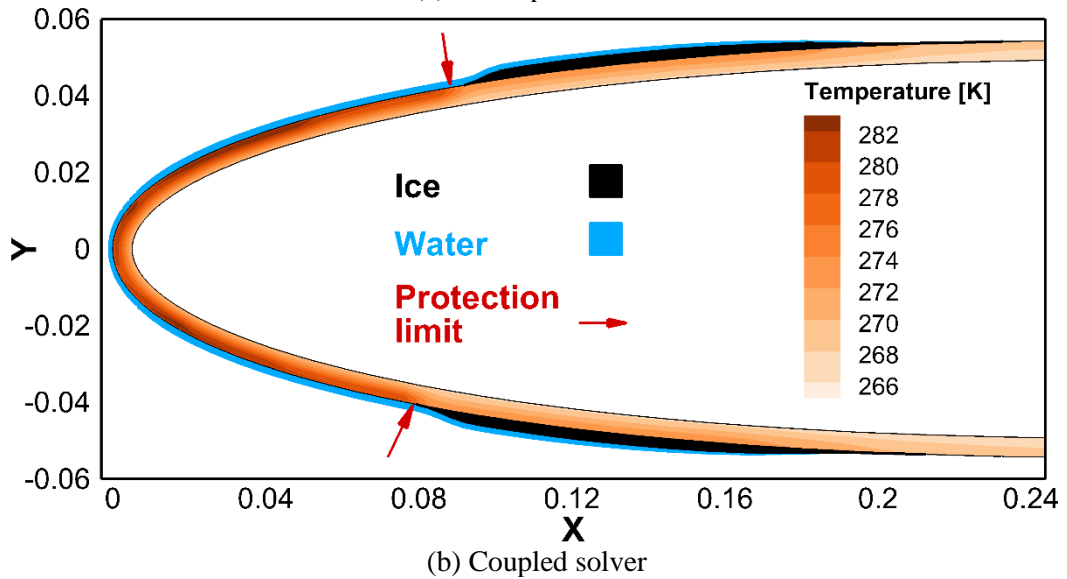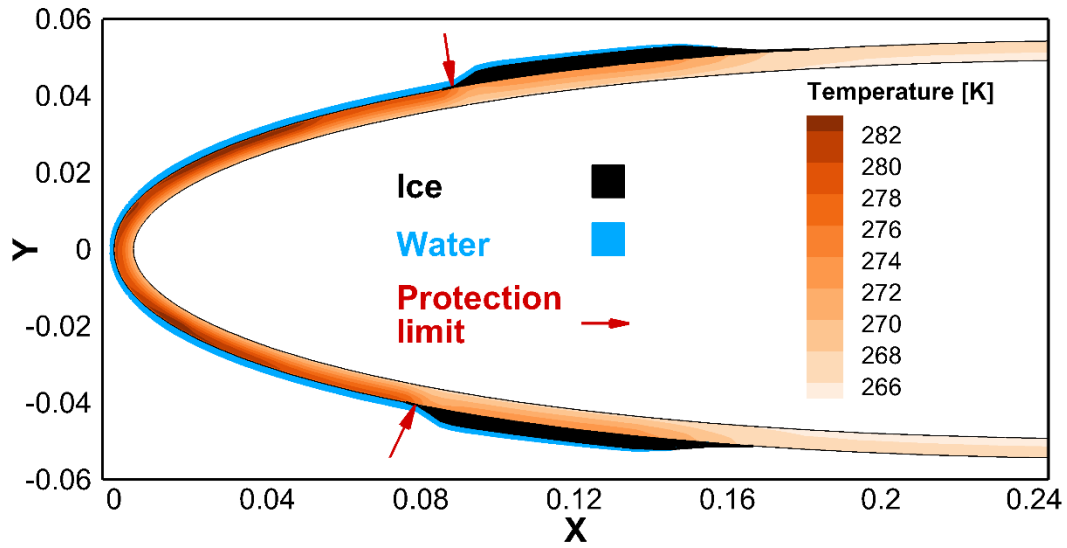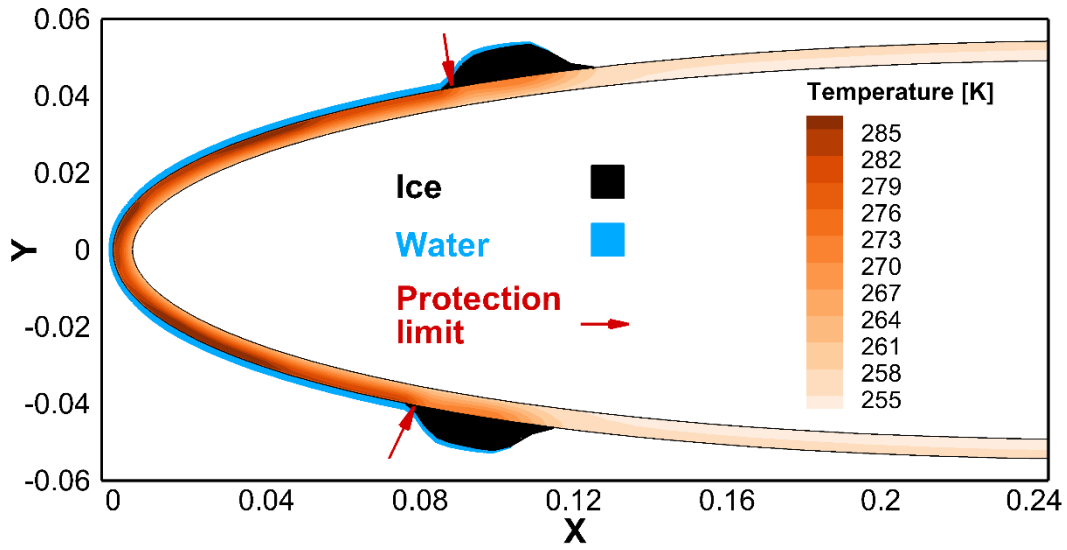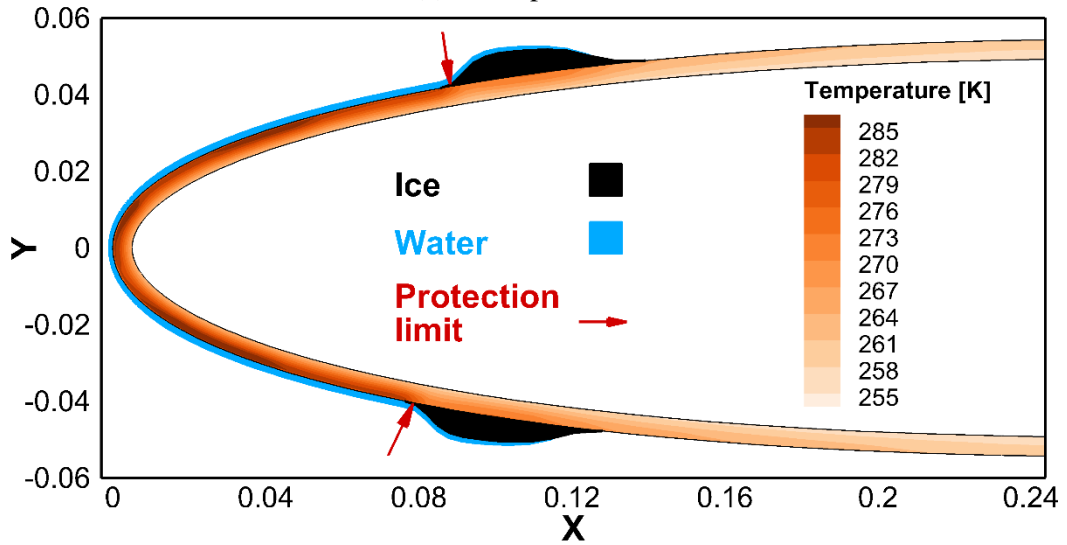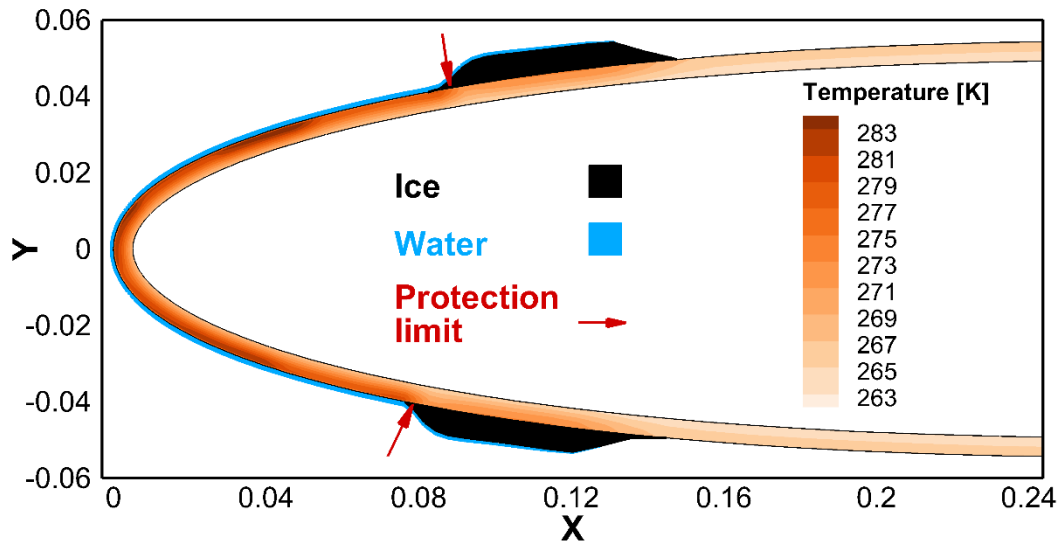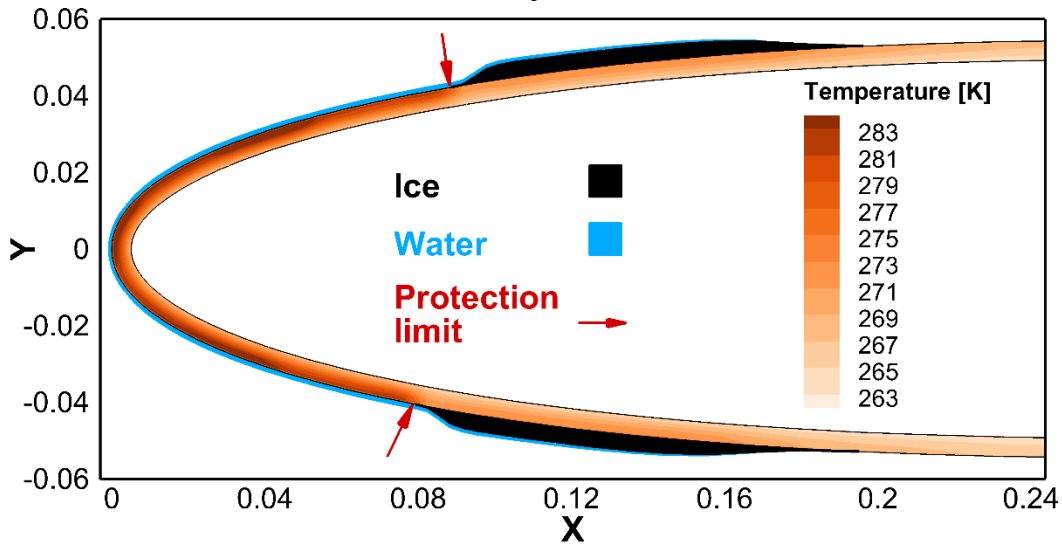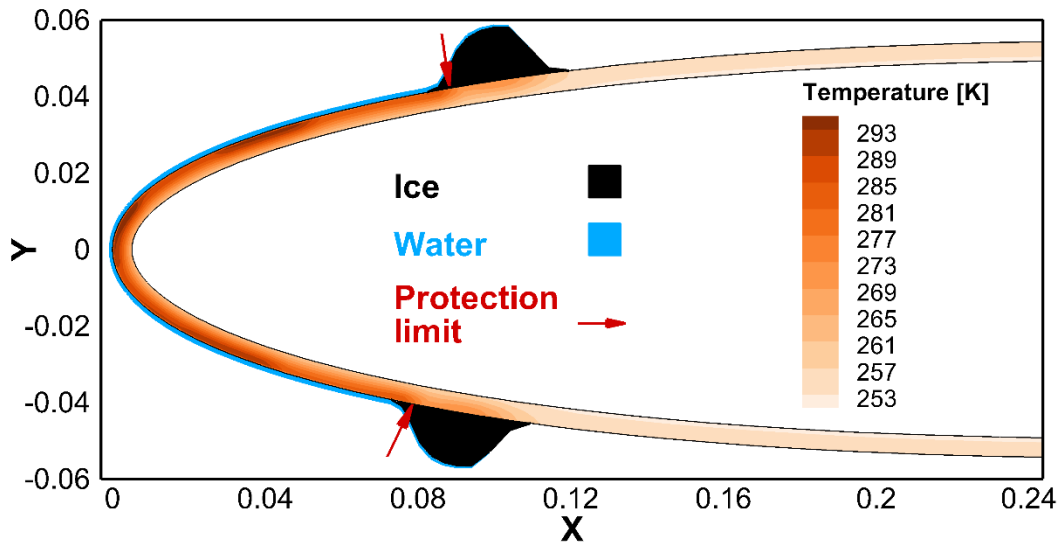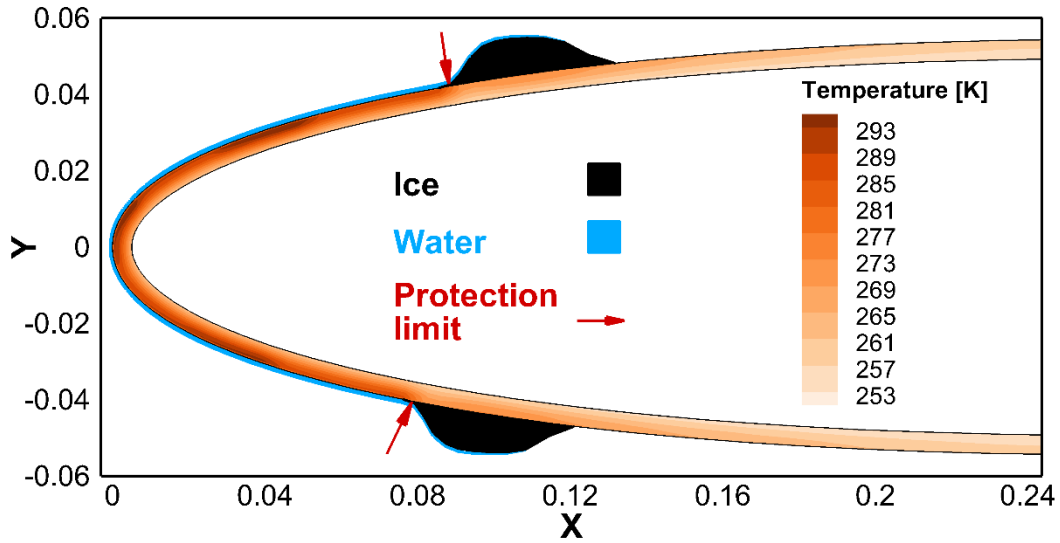

(a) Decoupled solver
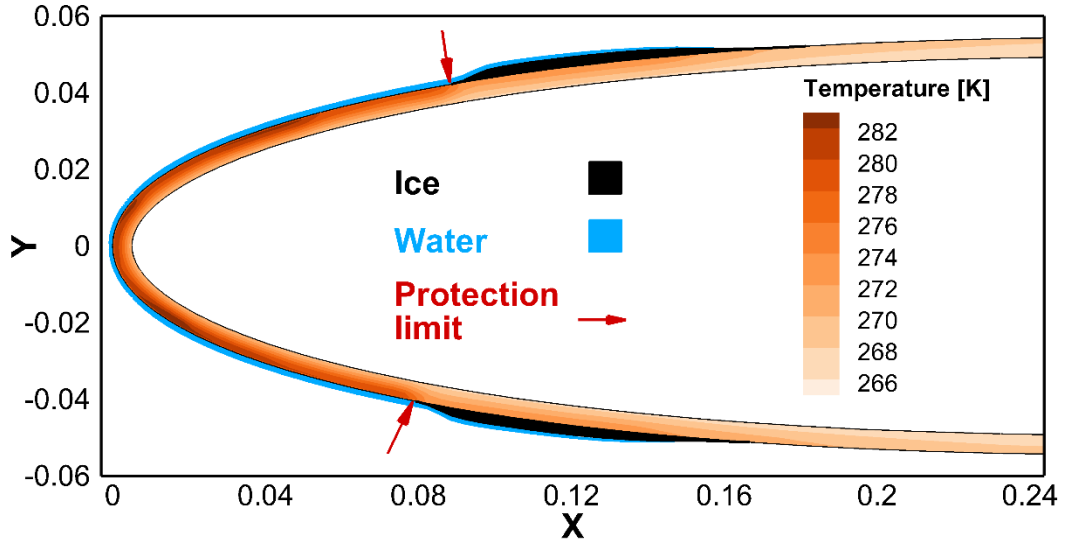
(b) Coupled solver

Fig. A1. Comparison of ice shape, water film, and temperature contours of (a) decoupled solver and (b) Coupled solver for case 22B, $T_\infty = 265.5K$, $U_\infty = 44.7 m/s$, $LWC = 0.78 g/m^3$, $AOA = 0°$. (For visualization purposes, the water film height was scaled up 100 times.)
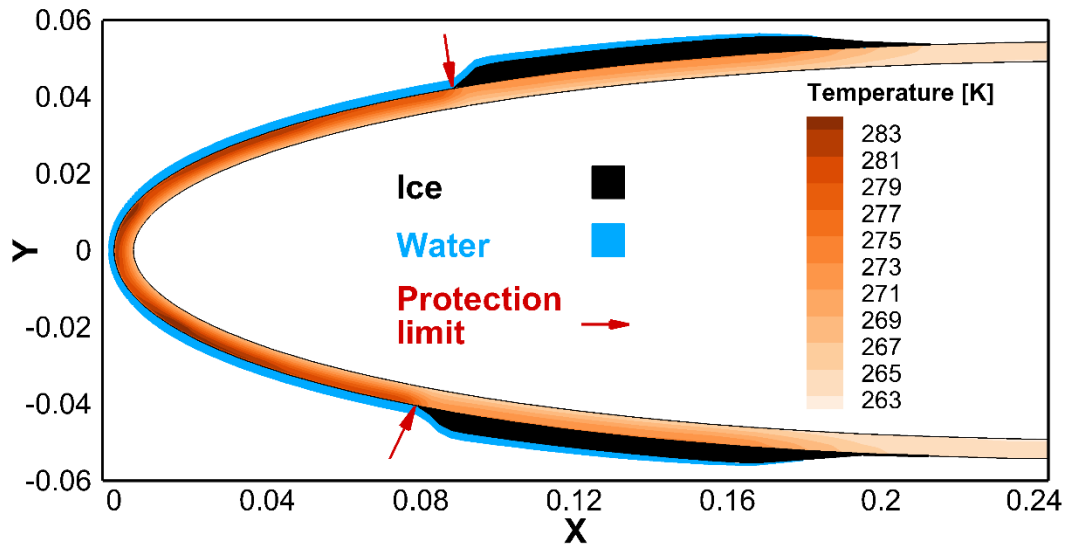
(a) Decoupled solver

(b) Coupled solver

Fig. A2. Comparison of ice shape, water film, and temperature contours of (a) decoupled solver and (b) Coupled solver for case 48B, $T_\infty = 265.5K$, $U_\infty = 44.7 m/s$, $LWC = 1.1 g/m^3$, $AOA = 0^\circ$. (For visualization purposes, the water film height was scaled up 100 times.)
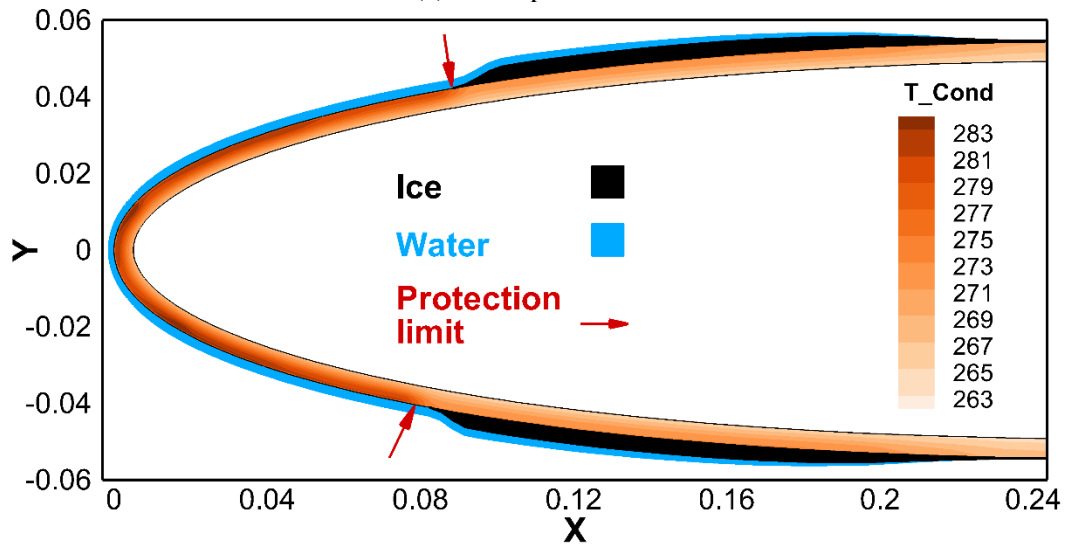
(a) Decoupled solver

(b) Coupled solver

Fig. A3. Comparison of ice shape, water film, and temperature contours of (a) decoupled solver and (b) Coupled solver for case 58B, $T_\infty = 254.4K$, $U_\infty = 44.7\,m/s$, $LWC = 1.1\,g/m^3$, $AOA = 0°$. (For visualization purposes, the water film height was scaled up 100 times.)
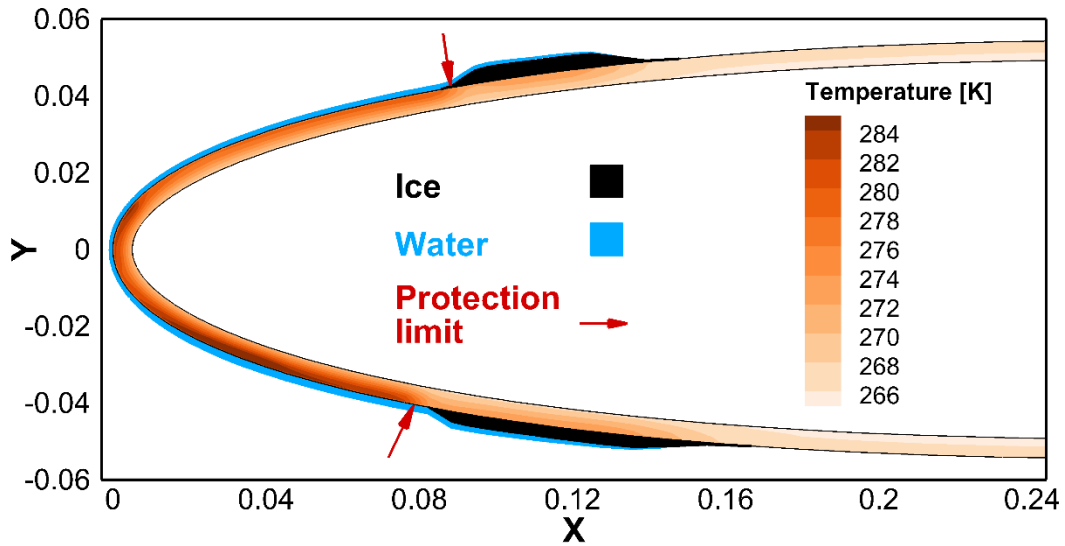
(a) Decoupled solver

(b) Coupled solver

Fig. A4. Comparison of ice shape, water film, and temperature contours of (a) decoupled solver and (b) Coupled solver for case 65B, $T_\infty = 262.5K$, $U_\infty = 89.4 m/s$, $LWC = 0.55 g/m^3$, $AOA = 0°$. (For visualization purposes, the water film height was scaled up 100 times.)
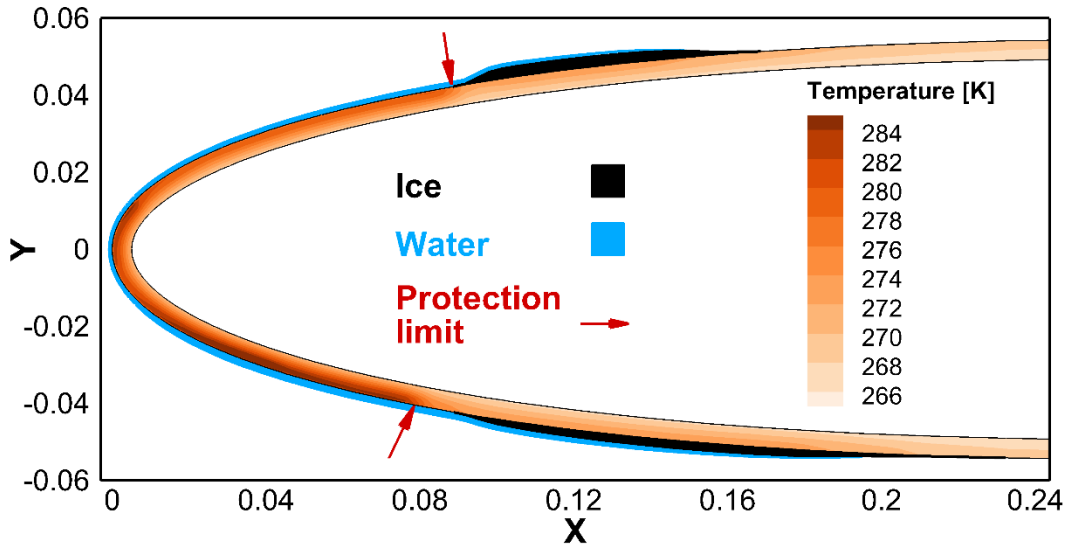
(a) Decoupled solver

(b) Coupled solver

Fig. A5. Comparison of ice shape, water film, and temperature contours of (a) decoupled solver and (b) Coupled solver for case 67B, $T_\infty = 251.4K$, $U_\infty = 89.4\,m/s$, $LWC = 0.55\,g/m^3$, $AOA = 0°$. (For visualization purposes, the water film height was scaled up 100 times.)
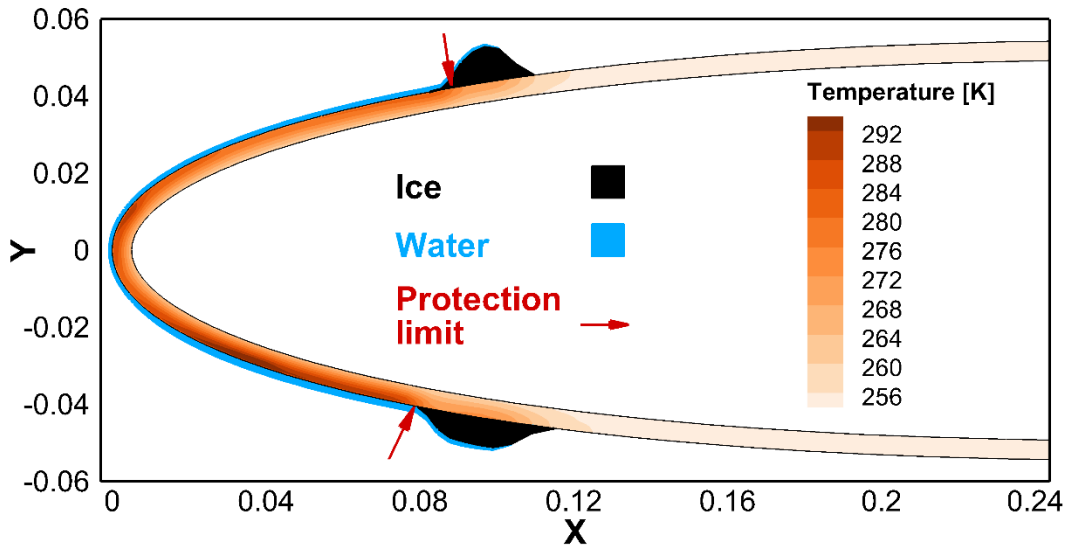
(a) Decoupled solver

(b) Coupled solver

Fig. A6. Comparison of ice shape, water film, and temperature contours of (a) decoupled solver and (b) Coupled solver for case 87B, $T_\infty = 262.7K$, $U_\infty = 44.7m/s$, $LWC = 2.0g/m^3$, $AOA = 0°$. (For visualization purposes, the water film height was scaled up 100 times.)
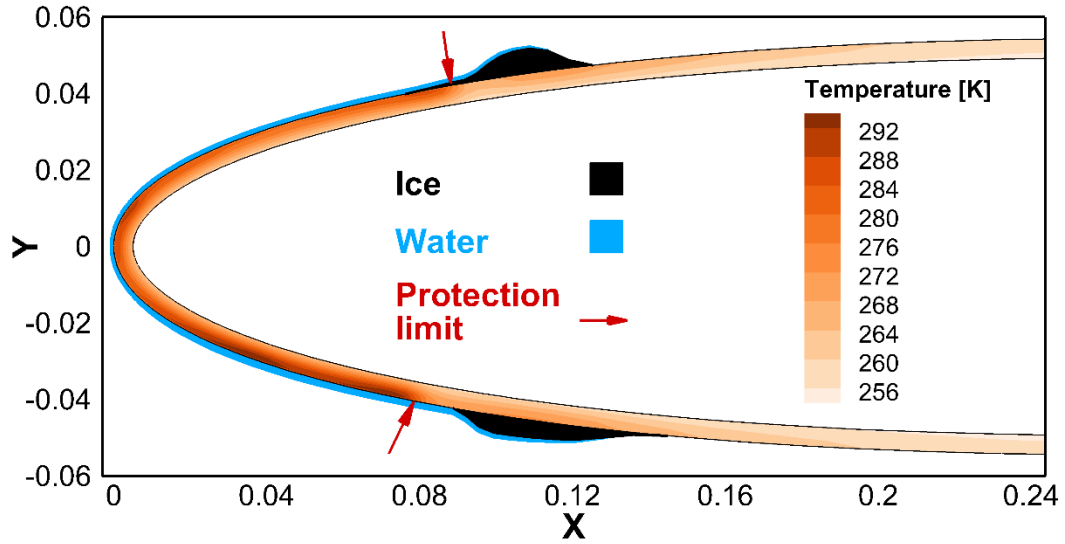
(a) Decoupled solver

(b) Coupled solver

Fig. A7. Comparison of ice shape, water film, and temperature contours of (a) decoupled solver and (b) Coupled solver for case 71B, $T_\infty = 265.5K$, $U_\infty = 44.7 m/s$, $LWC = 0.78 g/m^3$, $AOA = 4°$. (For visualization purposes, the water film height was scaled up 100 times.)

(a) Decoupled solver

(b) Coupled solver

Fig. A8. Comparison of ice shape, water film, and temperature contours of (a) decoupled solver and (b) Coupled solver for case 91B, $T_\infty = 254.4K$, $U_\infty = 44.7 \, m/s$, $LWC = 0.78 \, g/m^3$, $AOA = 4^\circ$. (For visualization purposes, the water film height was scaled up 100 times.)